1 **Pharmacological inhibition of bromodomain and extra-terminal proteins induces NRF-2-**

2 **mediated inhibition of SARS-CoV-2 replication and is subject to viral antagonism**

3 Baxolele Mhlekude[1,2], Dylan Postmus[1,2], January Weiner 3rd[2], Saskia Stenzel[1,2], Francisco J.

4 Zapatero-Belinchón[3,4,5], Ruth Olmer[6], Jenny Jansen[1,2], Anja Richter[1], Julian Heinze[1], Nicolas

5 Heinemann[1], Barbara Mühlemann[1], Simon Schroeder[1], Terry C. Jones[1,7], Marcel Alexander

6 Müller[1], Christian Drosten[1], Andreas Pich[8], Volker Thiel[9,10], Ulrich Martin[6], Daniela

7 Niemeyer[1], Gisa Gerold[3,4,5], Dieter Beule[2], Christine Goffinet[1,2*]

8 [1]Institute of Virology, Charité - Universitätsmedizin Berlin, corporate member of Freie

9 Universität Berlin, Humboldt-Universität zu Berlin, Charitéplatz 1, 10117 Berlin, Germany

10 [2]Berlin Institute of Health at Charité – Universitätsmedizin Berlin, Charitéplatz 1, 10117,

11 Berlin, Germany

12 [3]Department of Biochemistry, University of Veterinary Medicine Hannover, 30559 Hannover,

13 Germany

14 [4]Institute of Experimental Virology, TWINCORE, Centre for Experimental and Clinical

15 Infection Research; a joint venture between the Hannover Medical School and the Helmholtz

16 Centre for Infection Research, 30625 Hannover, Germany

17 [5]Department of Clinical Microbiology, Virology & Wallenberg Centre for Molecular Medicine

18 (WCMM), Umeå University, SE-90185 Umeå, Sweden

19 [6]Leibniz Research Laboratories for Biotechnology and Artificial Organs (LEBAO), Department

20 of Cardiothoracic, Transplantation and Vascular Surgery, REBIRTH - Center for Translational

21 Regenerative Medicine, Biomedical Research in Endstage and Obstructive Lung Disease

22 Hannover (BREATH), German Center for Lung Research (DZL), Hannover Medical School,

23 30625 Hannover, Germany

24 [7]Centre for Pathogen Evolution, Department of Zoology, University of Cambridge, Downing

25 St., Cambridge, CB2 3EJ, U.K.

26 [8]Institute of Toxicology, Hannover Medical School, Core Facility Proteomics, 30629

27 Hannover, Germany

28   [9]Institute of Virology and Immunology (IVI), University of Bern, 3001 Bern, Switzerland

29   [10]Department of Infectious Diseases and Pathobiology, Vetsuisse Faculty, University of Bern,

30   3001 Bern, Switzerland

31   *Corresponding author:

32   Christine Goffinet

33   Institute of Virology, Charité Campus Mitte, Charité - Universitätsmedizin Berlin, corporate

34   member of Freie Universität Berlin, Humboldt-Universität zu Berlin, Charitéplatz 1, 10117

35   Berlin, Germany

36   Phone: +49 30 450 525 489

37   Email: christine.goffinet@charite.de

38   **Keywords:**

39   BETs, iBETs, SARS-CoV-2, VOCs, NRF-2, antagonism

40   **ABSTRACT**

41   Inhibitors of bromodomain and extra-terminal proteins (iBETs), including JQ-1, have

42   been suggested as potential therapeutics against SARS-CoV-2 infection. However, molecular

43   mechanisms underlying JQ-1-induced antiviral activity and its susceptibility to viral

44   antagonism remain incompletely understood. iBET treatment transiently inhibited infection by

45   SARS-CoV-2 variants and SARS-CoV, but not MERS-CoV. Our functional assays confirmed

46   JQ-1-mediated downregulation of ACE2 expression and multi-omics analysis uncovered

47   induction of an antiviral NRF-2-mediated cytoprotective response as an additional antiviral

48   component of JQ-1 treatment. Serial passaging of SARS-CoV-2 in the presence of JQ-1

49   resulted in predominance of ORF6-deficient variants. JQ-1 antiviral activity was transient in

50   human bronchial airway epithelial cells (hBAECs) treated prior to infection and absent when

51   administered therapeutically. We propose that JQ-1 exerts pleiotropic effects that collectively

52   induce a transient antiviral state that is ultimately nullified by an established SARS-CoV-2

53   infection, raising questions on their clinical suitability in the context of COVID-19.

54   **INTRODUCTION**

55   There is an unmet need for novel effective therapies against the evolving variants of

56   severe acute respiratory syndrome coronavirus-2 (SARS-CoV-2), the causative agent of the

57   coronavirus disease-2019 (COVID-19) pandemic. The hallmark of severe SARS-CoV-2

58   infections is an excessive inflammatory response resulting in tissue damage and multiorgan

59   failure (Bülow Anderberg et al., 2021). Therefore, therapeutic avenues that simultaneously

60   dampen SARS-CoV-2 replication and antagonise its pathophysiological effects are utmostly

61   desired.

62   A group of small molecular inhibitors of the bromodomain and extra-terminal (BET)

63   proteins (iBETs) has been suggested to hold potential for the realisation of such therapies

64   (Gilham et al., 2021; Mills et al., 2021; Samelson et al., 2022; Vann et al., 2022). The BET

65   protein family is made up of four multifaceted, ubiquitously expressed and evolutionarily

66   conserved proteins: bromodomain-containing protein (BRD) BRD2, BRD3, BRD4, and BRTD

67   (Lara-Ureña and García-Domínguez, 2021). They act as epigenetic readers and transcriptional

68   co-activators by binding to the acetylated lysine residues in histones in the chromatin and

69   recruit the cellular transcriptional machinery to drive transcription of their target genes (Cheung

70   et al., 2021; Suarez-Alvarez et al., 2017). Alternatively, BET proteins can act as transcriptional

71   co-repressors by interacting with their cellular partners to form repressor complexes, which

72   suppress inappropriate transcriptional programs to maintain tissue homeostasis (Cheung et al.,

73   2021).

74   The ability of BET proteins to regulate transcription has made them prime targets for

75   several diseases that hijack the cellular transcriptional machinery, including SARS-CoV-2

76   infection (Chen et al., 2022; De Rijck et al., 2013; Gordon et al., 2020; Shorstova et al., 2021;

77   Wu et al., 2016). iBETs evict BET proteins from histones and their non-histone binding

78   partners (Stathis and Bertoni, 2018). Therefore, clinical development of iBETs, most of which

79   are in different phases of clinical trials in the context of cancer therapy and other pathologies

80   (Hajmirza et al., 2018; Shorstova et al., 2021), may provide a pharmacological tool for

81   therapeutic intervention against several diseases driven by the BET protein-mediated

82   transcriptional programs.

83   BRD2 co-activates expression of ACE2 (Samelson et al., 2022), the main receptor for

84   SARS-CoV-2 entry into target cells (Hoffmann et al., 2020). Consequently, treatment of target

85   cells with iBETs downregulates ACE2 expression and inhibits SARS-CoV-2 replication and

86   inflammatory responses (Gilham et al., 2021; Mills et al., 2021; Samelson et al., 2022).

87   Additionally, BET proteins co-activate the interferon (IFN) (Patel et al., 2013) and NF-κB

88   (Huang et al., 2009) signalling pathways, which are the main drivers of the inflammatory

89   responses in COVID-19 patients (Lee et al., 2020; Ramasamy and Subbian, 2021).

90   Despite the growing literature on the anti-SARS-CoV-2 activity of iBET candidates

91   (Gilham et al., 2021; Mills et al., 2021; Samelson et al., 2022; Vann et al., 2022), key questions

92   remain regarding the genome-wide epigenetic alterations orchestrating iBET-mediated

93   transcriptional responses that underlie their anti-SARS-CoV-2 activity. The missing

94   information about the susceptibility of iBET-mediated antiviral activity to SARS-CoV-2

95   subversion is hampering their potential as the next generation of prophylactics in the context of

96   COVID-19. Here, we sought to address these key questions by conducting an in-depth

97   functional and multi-omics analysis of the signalling alterations that underlie JQ-1-mediated

98   anti-SARS-CoV-2 activity.

99   **MATERIALS & METHODS**

100   **Chemicals and inhibitors**

101   (+)-JQ-1 (Cat no. SML1524-5MG) was purchased from Sigma. ABBV-075 (Cat no.

102   S8400) (ClinicalTrails.gov Identifier: NCT02391480), OTX015 (Cat no. S7360)

103   (ClinicalTrails.gov Identifier: NCT02698176), ARV-825 (Cat no. S8297) and ML385 (Cat no.

104   S8790) were purchased from Selleckchem. Dimethyl sulfoxide (DMSO) (Item no. 10127403)

105   was purchased from Thermo Fisher Scientific.

106   **Cell lines**

107   Calu-3 (ATCC HTB-55), CaCo-2 (ATCC HTB-37), Vero E6 (ATCC CRL-1586) and

108   parental HEK293T cells (ATCC CRL-3216) were cultured in Dulbecco's Modified Eagle's

109   Medium (DMEM) supplemented with 10% heat-inactivated fetal calf serum (FCS), 100 U/ml

110   Penicillin-Streptomycin and 2mM L-glutamine (Gibco, UK) (hereafter referred to as 10%

111   DMEM) at 37°C/5% CO_2. Primary bronchial airway epithelial cells were cultured in air-liquid

112   interface (ALI) mode in the provided ALI medium at 37 °C/5% CO_2. Unless stated otherwise,

113   all cell cultures were maintained at 37°C/5% CO_2.

114   **Human bronchial airway epithelial cells (Air-liquid interface cultures)**

115   Human bronchial airway epithelial cells (hBAECs) were isolated from explanted lungs

116   obtained from the Hannover Lung Transplant Program after patients' informed consent, ethical

117   vote 2923-2015. For isolation of hBAECs, human bronchial tissue was cut into small pieces in

118   Hank's buffer (Thermo Fisher Scientific) containing 0.18% protease XIV and incubated for

119   two hours at 37°C. After thorough pipetting with a 25/50 ml serological pipette, cell solution

5

120   was filtered through a 100 µm cell strainer (Corning) to remove clumps and 10 ml RPMI

121   supplemented with 10% FCS (Thermo Fisher Scientific) was added. After centrifugation for 10

122   min at 500g and 4°C, supernatant was removed and cells were resuspended in SAEGM^{TM}

123   (PromoCell) + Primocin (InvivoGen) + Penicillin-Streptomycin (P/S) (Sigma-Aldrich). For

124   ALI cultures, 200,000 hBAECs were seeded onto PureCol- (Advanced BioMatrix) coated 12-

125   well inserts (Greiner Bio-One) in SAEGM^{TM} + Primocin + P/S. 48 hours post seeding, culture

126   medium in apical and basal chambers was changed to PneumaCult-ALI medium (STEMCELL

127   Technologies). Air lift was performed 48 hours later by gently removing medium from the

128   apical chamber. Homogenous distributed cilia were visible three weeks after air lift and inserts

129   were used for infections.

130   **Cell viability assays**

131   Calu-3 cells (6×10^5 cells/ml) seeded overnight in 96-well plates were treated with serial

132   dilutions (prepared in culture medium) of the iBETs or corresponding DMSO controls for 72

133   hours; with PBS wash, medium change and fresh drug administration after every 24 hours.

134   Post-treatment, cells were subjected to viability assays using the CellTiter-Glo Luminescent

135   Cell Viability Assay Kit (Promega, Germany) for Calu-3 cells and CellTiter-Glo 3-D Cell

136   Viability Assay Kit (Promega, Germany) for hBAECs according to the manufacturer's

137   protocol. The raw data from the test samples were background subtracted, normalised to naïve

138   cells, and analysed using GraphPad Prism v9 (LaJolla, CA, USA) as previously described

139   (Mhlekude et al., 2021).

140   **Virus production**

141   SARS-CoV-2 (passage (P) 1, BetaCoV/Munich/BavPat1/2020|EPI_ISL_406862)

142   (Wölfel et al., 2020), SARS-CoV (P1, HKU-39849 Hong Kong) (Lau et al., 2005; Zeng et al.,

143   2003), and MERS-CoV (P2, EMC/2012) (Zaki et al., 2012) stocks were propagated in Vero E6

144   cells to generate P2, P2, and P3 stocks respectively. The virus stock production and quality

145   control by Next Generation Sequencing were conducted as previously described (Niemeyer et

146   al., 2021). All infectious pathogens were handled under biosafety level three (BSL-3)

147   conditions with respiratory personal protection equipment.

148   **Virus infection of Calu-3 cells**

149   Calu-3 cells (6×10^5 cells/ml) seeded overnight in 12-well plates were treated with serial

150   dilutions of iBETs or corresponding DMSO controls for 48 hours; with PBS wash, medium

151   change and fresh drug administration every 24 hours. Post-treatment, cells were inoculated with

152   viruses (SARS-CoV and SARS-CoV-2, MOI 0.1; and MERS-CoV, MOI 0.0005) and incubated

153   for one hour. After infection, cells were washed with PBS, supplied with fresh medium and

154   iBETs and incubated for 24 hours. The next day, 50 µl of supernatant was collected into 300 µl

155   of RAV1 lysis buffer (Machery-Nagel, Germany) for viral RNA extraction and 100 µl into 100

156   µl of 0.5% gelatine medium for plaque assays. Cells were washed with PBS, trypsinized and

157   reconstituted in culture medium, from which 50 µl was collected into 300 µl of RAV1 lysis

158   buffer (Machery-Nagel, Germany) to isolate cell-associated RNA. RNA samples were stored at

159   -20°C and plaque assay samples at -80°C until sample processing.

160   **Virus infection of human bronchial airway epithelial cells (hBAECs)**

161   JQ-1 or DMSO was added into the culture medium (PneumaCult-ALI) in the basal

162   compartment of cells cultured in transwells and incubated for 48 hours, followed by medium

163   exchange and new drug administration after 24 hours as mentioned above. Post-treatment, cells

164   were washed three times with pre-warmed PBS to remove mucus from the apical compartment

165   and inoculated with SARS-CoV-2 ($2x10^4$ PFU diluted in OptiPRO medium), followed by

166   incubation for 90 minutes. The inoculum was then aspirated and cells washed with PBS three

167   times. The transwells were then transferred into new plates with the drug-containing culture

168   medium. To harvest samples for zero time point, 200 µl of culture medium was immediately

169   added onto the cells in the apical compartment and incubated for 15 min to elute the virus

170   particles. Following incubation, 50 µl of virus eluate was collected into 300 µl RAV1 lysis

171   buffer (Machery-Nagel, Germany) for viral RNA extraction and 100 µl into 100 µl of 0.5%

172   gelatine medium for plaque assays, after which the eluate residues were aspirated from the

173   apical compartment and followed by incubation of cells. This harvesting procedure was

174   repeated every 24 hours for kinetic experiments. The samples were stored at -20°C and -80°C,

175   respectively, until processing.

176   **Quantitative real-time PCR**

177   Viral RNA from the supernatant was extracted using the NucleoSpin RNA Virus

178   Isolation Kit (Macherey-Nagel, Germany) according to the manufacturer's protocol. To

179   quantify viral RNA copies, a 12.5 µl reaction/well was prepared in 4titude® 96-Well Semi-

180   Skirted PCR Plates for LC480 (Roche) using a SuperScript III One-Step RT-PCR Kit

181   (Invitrogen, Germany). Reverse transcription of the viral RNA and amplification of the cDNA

182   was conducted in a LightCycler 480 System (Roche, Germany) using the following protocol:

183   55°C, 10 min; 95°C, 3 min; 95°C, 15 sec; 58°C, 30 sec and 40°C, 30 sec for 45 cycles and

184 qPCR primers against SARS-CoV and SARS-CoV-2 E gene and probes (Corman et al., 2020).

185 The absolute quantification of the viral RNA copies was calculated by a standard curve method

186 using viral RNA standards (Corman et al., 2020).

187 **Plaque titration assays**

188 Seeded Vero E6 cells (4 x 10^5 cell/ml) were left overnight in 24-well plates. The virus-

189 containing samples (50 µl) were serially diluted in 450 µl aliquots of serum-free Opti-Pro

190 medium (Gibco, UK), after which 200 µl from each dilution were added in duplicates to the

191 cells, followed by one hour incubation. Post-infection, viral inoculum was aspirated from the

192 cells, cells washed with PBS, and overlaid with 2.4% Avicel (FMC BioPolymers, Germany)

193 mixed with 2xDMEM (1:1 ratio), followed by incubation for 72 hours. The overlay was

194 aspirated from the cells, after which they were fixed for 30 min with 6% formaldehyde and

195 stained with crystal violet solution (0.2% crystal violet, 2% ethanol and 10% formaldehyde) for

196 20 min. Plaque Forming Units (PFU) were determined from at least two dilutions for which

197 distinct plaques were detectable and expressed as PFU/ml.

198 **Flow cytometry**

199 JQ-1 and DMSO-treated Calu-3 cells were infected with GFP-tagged SARS-CoV-2

200 (synSARS-CoV-2-GFP-P2A-ORF7a clone #41, (Thi Nhu Thao et al., 2020) (MOI 0.25)

201 following the above-mentioned protocol. Subsequently, cells were trypsinized, PBS-washed

202 and fixed for 90 minutes with 4% PFA. GFP signal was quantified by flow cytometry in

203 FACSCelesta (BD Bioscience, Germany) and analysed by FlowJo v10.8 (Tree Star, Ashland,

204 Oregon, USA).

205 **Immunoblotting**

206 Calu-3 cells were lysed in 60 µl RIPA Lysis Buffer (Thermo Fisher Scientific,

207 Germany) supplied with 1 % Protease Inhibitor Cocktail Set III (Merck Chemicals, Germany)

208 for 30 min at 4 °C. Subsequently, cell lysates were pelleted and protein concentration in

209 supernatant was determined by BCA protein assay (ThermoFisher Scientific). 20 µg total

210 protein from each sample was mixed with 4x Laemmli buffer, which was supplemented with

211 10% beta-mercaptoethanol, then boiled for ten minutes at 95°C to ensure protein denaturation.

212 Proteins were resolved on 6% SDS-PAGE gel and transferred to a nitrocellulose membrane

213 (0.45 µm pore size, GE Healthcare) by Trans-Blot Turbo system (BioRad). Membranes were

214 blocked with 5% dried milk in 0.1% PBS-Tween (0.9% NaCl, 10 mM Tris-HCl [pH 7.5], 0.1%

215 Tween 20) for 30 min at room temperature. Blocked membranes were incubated with the

216   primary antibodies against ACE2 (#AF933, R&D Systems) and beta-actin (#A5316, Sigma-

217   Aldrich). Secondary antibodies conjugated with horseradish peroxidase (HRP) were used for

218   chemiluminescence-based detection by Fusion Fx7 (Peqlab Biotechnologie GmbH). Detection

219   was performed using SuperSignal™ West Femto substrate (ThermoFisher Scientific).

220   **Production of pseudotyped lentivirus particles and transduction assays**

221   SARS-CoV-2-S- and VSV-G-pseudotyped lentiviral particles (Hu et al., 2020) were

222   produced by calcium phosphate-based transfection of HEK293T cells with the packaging

223   plasmid pCMV ΔR8.91 (Zufferey et al., 1997), the lentiviral transfer plasmid pCSII-EF-

224   luciferase (Agarwal et al., 2006), and pCMV-VSV-G (Stewart et al., 2003) using the CalPhos

225   Mammalian Transfection Kit (Takara Bio Company, Germany) according to the manufacturer's

226   protocol. Dose-dependent treatment of Calu-3 cells with JQ-1, followed by transduction with

227   pseudovirus particles in 96-well plates was conducted under BSL-2 conditions, after which the

228   infection efficiency was analysed luminometrically in Synergy™ HTX Multi-Mode Microplate

229   Reader (BioTek Instruments, Inc.) using the Luciferase Assay System (Promega, Germany)

230   according to the manufacturer's protocol.

231   **ATAC-seq**

232   Bulk ATAC-seq and RNA-seq were conducted in parallel from the identical infection

233   experiment. Calu-3 cells were treated with JQ-1 and DMSO, respectively, for 24 hours,

234   infected with SARS-CoV-2 (MOI 0.1) under continuous treatment for another 24 hours.

235   Uninfected but treated, and naïve Calu-3 cells were used as reference. Post-infection, ATAC-

236   seq libraries were prepared from 50,000 cells per replicate using Illumina Tagment DNA

237   Enzyme and Buffer Kit (Illumina 20034197) according to the Omi-ATAC-seq protocol (Corces

238   et al., 2017) with the following minor optimizations. Briefly, 5 µl from the partially amplified

239   barcoded fragments was subjected to SYBR Green qPCR in a LightCycler 480 System (Roche,

240   Germany) using the FastStart Essential DNA Green Master Mix (Roche, Germany) according

241   to the manufacturer's protocol. Amplification was conducted for 20 cycles using a universal

242   forward primer and the sample-specific barcoded reverse primers (Buenrostro et al., 2013).

243   Amplification curves from SYBR Green qPCR were generated and used to determine the

244   number of cycles that give ⅓ of the maximum fluorescence. Final library preparation was

245   conducted by conventional PCR for 8-12 cycles. The amplified libraries were subjected to a

246   single left-sided bead purification using the AMPure XP magnetic beads (Beckman Coulter,

247   Germany). Libraries were sequenced on SP lane of NovaSeq 6000 System (Illumina) at the

248 MDC/BIH Genomic Core Facility to generate 40 million 75-nucleotide paired-end reads per
249 sample.

RNA-seq

251 Total RNA was isolated from $3x10^5$ cells per replicate using Direct-Zol RNA Miniprep
252 Kit (Zymo Research, USA) according to the manufacturer's protocol and shipped in dry ice to
253 the MDC/BIH Genomic Core Facility for quality assessment using TapeStation (Agilent
254 Technologies). Libraries were prepared using TrueSeq Stranded mRNA kit to generate
255 Illumina-compatible libraries by following the manufacturer's protocol (Illumina). Libraries
256 were sequenced on SP lane of NovaSeq 6000 System (Illumina) to generate 40 million 75-
257 nucleotide paired-end reads per sample.

Liquid chromatography tandem mass spectrometry (LC-MS/MS)

259 Treatment of Calu-3 cells and infection with SARS-CoV-2 were performed following
260 the above-mentioned protocol. Treated but uninfected and naïve cells served as references.
261 Preparation of cell lysate samples and protein quantification were conducted as mentioned
262 above, from which 50 µg of proteins per sample were prepared and resolved on 7.5% linear
263 SDS-PAGE gels as described elsewhere (Mhlekude et al., 2021). The in-gel protein digestion
264 and liquid chromatography coupled with tandem mass spectrometry (LC-MS/MS) experiments
265 were performed as previously described (Jochim et al., 2011)**.**

Bioinformatics analysis

267 For RNA-seq, reads were aligned to the human genome version GRCh38 and counted
268 using STAR (Dobin et al., 2013). Differential expression analysis was conducted using
269 DESeq2 version 1.30 (Love et al., 2014). Transcription factor analysis was performed using the
270 R package Dorothea (Garcia-Alonso et al., 2019) For ATAC-seq, reads were aligned to the
271 human genome GRCh38, after which the peaks were called using MACS2 v. 2.2.7.1 (Zhang et
272 al., 2008). For differential TF binding analysis, the R package DiffBind v. 3.0.15 (Stark and
273 Brown) was used. Motif search analysis was performed using the MEME suite (Bailey et al.,
274 2015) and DREME (https://meme-suite.org/meme/doc/dreme.html). Gene set enrichment
275 analysis was performed with the R package cluster Profiler v. 3.18 (Yu et al., 2012). All results
276 were corrected for multiple testing using the Benjamini-Hochberg procedure (Benjamini and
277 Hochberg, 1995). Genes were annotated as involved in IFN signalling, the cell cycle, or
278 autophagy by referring to the Reactome Interferon Signalling geneset (R-HSA-913531), the
279 Reactome Cell Cycle geneset (R-HSA-1640170), and the KEGG Autophagy - animal geneset

280   (hsa04140), respectively. Genes identified as targets for NRF2 signalling were identified based

281   on a previous report (Olagnier et al., 2020). LC-MS/MS data analysis was conducted as

282   previously described (Mhlekude et al., 2021).

283   **Statistical analysis**

284   If not stated otherwise, bars show the arithmetic mean of indicated amount of

285   repetitions. Error bars indicate standard error of the mean (SEM) from the indicated amount of

286   individual experiments. Statistical significance was calculated by performing a Student's t-test

287   using GraphPad Prism. P values ≤ 0.05 were considered significant: $\square 0.05$ (*), $\square 0.0021$ (**),

288    $\square 0.0002$ (***), $\square 0.0001$ (****) and n.s. = not significant (≥ 0.05).

289   **Data and code availability**

290   All code used to perform the analysis of the RNAseq and ATACseq data will be

291   available at https://github.com/GoffinetLab/SARS-CoV-2_JQ1-Antiviral-Study. Raw and

292   processed OMICs data will be deposited on the GEO database.

293   **RESULTS**

294   **Prophylactic administration of inhibitors of bromodomain and extra-terminal proteins**

295   **(iBET) inhibit SARS-CoV-2 infection in lung epithelial Calu-3 cells**

296   Inhibition of SARS-CoV-2 infection by several iBET compounds has been reported in different

297   infection models (Gilham et al., 2021; Mills et al., 2021; Samelson et al., 2022). To gain more

298   insights into their antiviral potency in the context of SARS-CoV-2 infection, we compared

299   antiviral activity of four iBETs, three (JQ-1, ABBV-075, and OTX-015) of which compete with

300   the acetylated molecules for binding to the bromodomains of the BET proteins, and one (ARV-

301   825) that targets BET proteins (dBET) carrying proteolysis-targeting chimera (PROTAC)

302   sequences to proteasomal degradation. iBET treatment of Calu-3 cells prior to SARS-CoV-2

303   infection led to a dose-dependent reduction of viral genomic RNA quantities (Fig. 1A and Sup.

304   Fig. 1C) and infectious titers (Fig. 1B and Sup. Fig. 1D) in the supernatant in the absence of

305   detectable cell toxicity (Sup. Figs. 1A and 1E). Of the investigated iBET candidates, JQ-1 (IC_{50}

306   = 0.290 μM) and ABBV-075 (IC_{50}=0.132 μM) were more potent than OTX-015 (IC_{50} = 3.553

307   μM) and ARV-825 (IC50 = 1.431 μM) against SARS-CoV-2 infection in Calu-3 cells.

308   Prophylactic administration of JQ-1 to hBAECs reduced SARS-CoV-2 viral RNA quantities by

309   24.8-fold (Fig. 1C) and infectious titers by 28.2-fold (Fig. 1D) without detectable toxicity (Sup.

310   Fig. 1B), demonstrating the relevance of iBET-mediated anti-SARS-CoV-2 activity in a

311   physiologically relevant primary cell model (Samelson et al., 2022). JQ-1 treatment rendered

312   Calu-3 cells 2.7-fold less susceptible to infection by recombinant GFP-expressing SARS-CoV-

313   2, reflecting the consistency of JQ-1-mediated anti-SARS-CoV-2 activity across different

314   readouts (Fig. 1E-F).
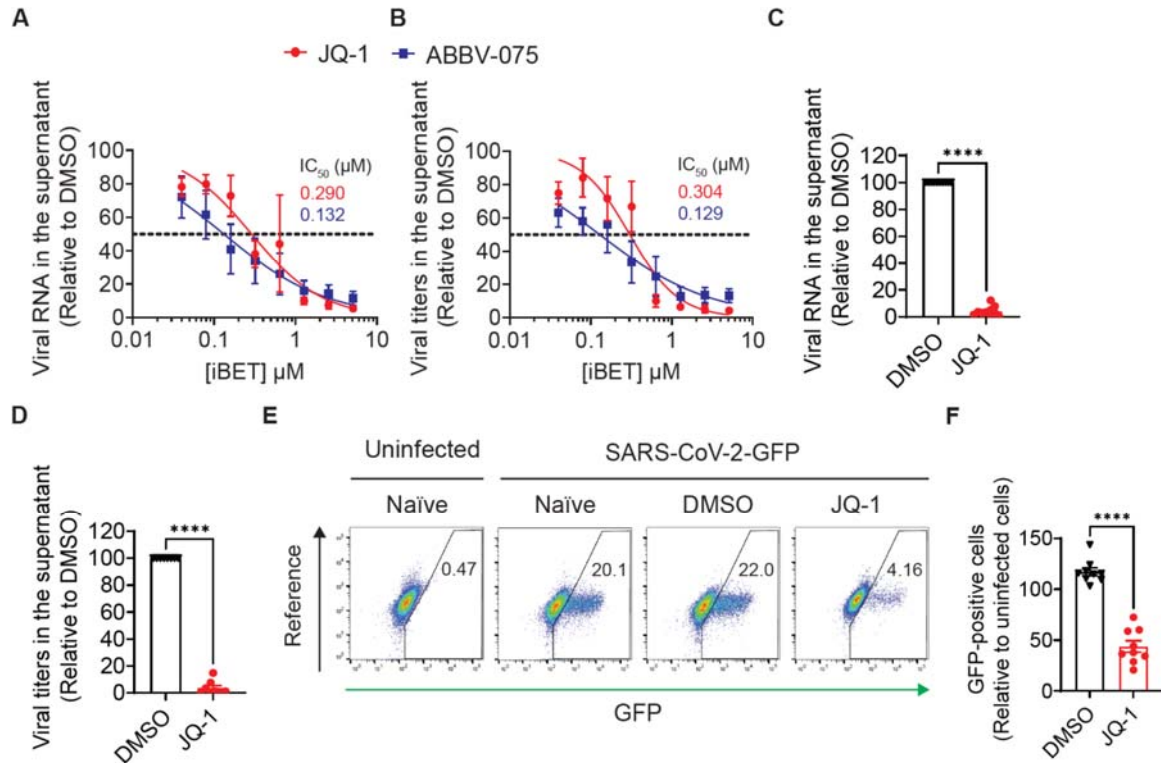
315
316   **Figure 1. Prophylactic administration of inhibitors of bromodomain and extra-terminal**

317   **proteins (iBET) inhibit SARS-CoV-2 infection in lung epithelial Calu-3 cells.**

318   (**A**-**B**) Calu-3 cells were pretreated with indicated concentrations of iBETs for 48 hours,

319   followed by infection with SARS-CoV-2 (MOI 0.1) under continuous presence of the drug. At

320   24 hours post infection, relative (**A**) SARS-CoV-2 RNA and (**B**) infectious titers in

321   supernatants were quantified from three independent experiments.

322   (**C**-**D**) hBAECs were pretreated with JQ-1 (2.56 µM) for 48 hours, followed by infection with

323   SARS-CoV-2 (2×10^4 PFUs) under continuous presence of the drug. At 48 hours post-infection,

324   (**C**) abundance of viral RNA from duplicates of five independent experiments and (**D**)

325   infectivity from duplicates of four independent experiments were quantified in supernatants.

326   Data shown are relative to DMSO treatment.

327   (**E**-**F**) Calu-3 cells were pretreated with JQ-1 for 48 hours prior to infection with a recombinant,

328   GFP-expressing SARS-CoV-2 (MOI 0.25). Shown are (**E**) representative FACS dot plots and

329   (**F**) quantification of percentage of GFP-positive cells relative to DMSO treatment at 24 hours

330   post infection, from three independent experiments with triplicates each. Unpaired

331   nonparametric Student *t*-test was used to compare the means between the experimental groups.

332   Error bars represent the arithmetic mean±SEM.

333   **JQ-1 exhibits a subgenera-specific antiviral activity among *Betacoronaviridae* in lung**

334   **epithelial Calu-3 cells**

335   To investigate whether the iBET-mediated anti-SARS-CoV-2 activity extends beyond SARS-

336   CoV-2 parental strains, which have been the main focus of the previous studies (Gilham et al.,

337   2021; Mills et al., 2021; Samelson et al., 2022), we compared the antiviral potency of JQ-1 in

338   Calu-3 cells infected with a panel of ß-coronaviruses. JQ-1 potently and dose-dependently

339   inhibited infection by SARS-CoV, SARS-CoV-2$_{B.1}$, SARS-CoV-2$_{B.1.1.7}$ and SARS-CoV-2$_{BA.2}$,

340   in contrast to MERS-CoV, as indicated by the reduction of viral RNA copies (Fig. 2A) and

341   infectious titers (Fig. 2B) in culture supernatants. These data suggest that JQ-1 exhibits a

342   subgenera-specific antiviral activity, which is directed towards infection by *Sarbecoviruses* and

343   not *Merbecoviruses* to which MERS-CoV belongs.
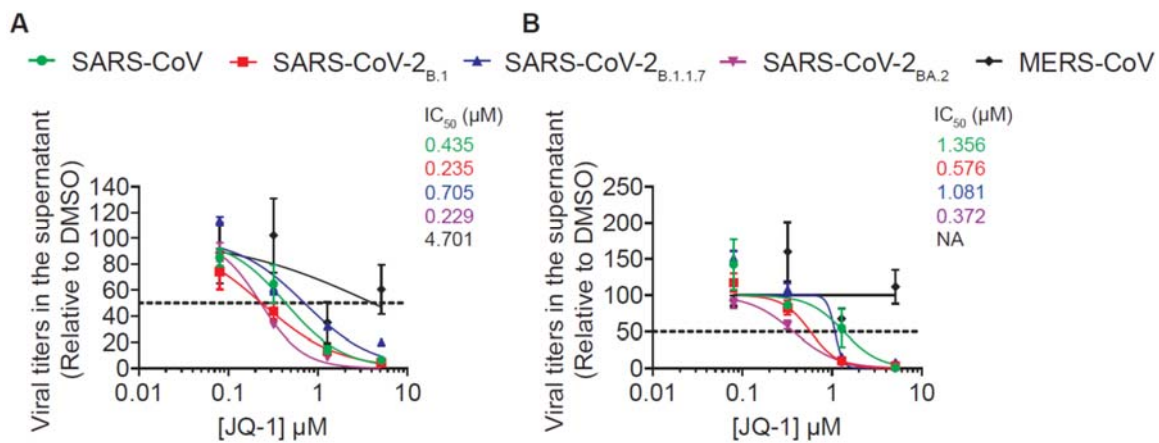
345   **Figure 2. JQ-1 exhibits a subgenera-specific activity among *Betacoronaviridae* in lung**

346   **epithelial Calu-3 cells.**

347   Calu-3 cells were pretreated with indicated concentrations of JQ-1 prior to infection with

348   indicated viruses. Shown are DMSO-normalised (**A**) viral RNA abundance and (**B**) infectivity

349   in supernatants harvested at 24 h.p.i. with *Sarbecoviruses* (MOI 0.1) and *Merbecovirus* (MOI

350   0.0001). Error bars represent the mean±SEM.

351   **JQ-1 exhibits a cell-directed anti-SARS-CoV-2 activity in lung epithelial Calu-3 cells**

352   Next, we compared the effect of JQ-1-mediated anti-SARS-CoV-2 activity when administered

353   prophylactically and at the time point of infection. Focusing on a single round of infection, we

354   found that JQ-1 inhibited SARS-CoV-2 replication when administered prophylactically in

355   Calu-3 cells, while it failed to inhibit infection when administered to cells during infection (Fig.

356   3A). PCR-based quantification of viral RNA copies showed that JQ-1-mediated reduction of

357   viral RNA copies in the supernatant of infected Calu-3 cells is accompanied by, and probably a

358   consequence of, reduced quantities of cell-associated viral RNA (Fig. 3B). The ratio of

359   extracellular to total viral RNA indicated that JQ-1 impaired release of SARS-CoV-2 virions

360   (Fig. 3C), without *per se* reducing the specific particle infectivity of secreted particles (Fig.

361   3D). In accordance with previous reports (Gilham et al., 2021; Mills et al., 2021; Samelson et

362   al., 2022), JQ-1 treatment reduced steady-state levels of ACE2 expression (Fig. 3E), an

363   observation that was accompanied by reduced susceptibility of Calu-3 cells to transduction with

364   SARS-CoV-2 spike, but not VSV-G-pseudotyped lentiviral particles (Sup. Fig. 3F). Together,

365   these data suggest that JQ-1 exhibits a cell-directed anti-SARS-CoV-2 activity involving, but

366   likely not restricted to, downregulation of ACE2 expression.
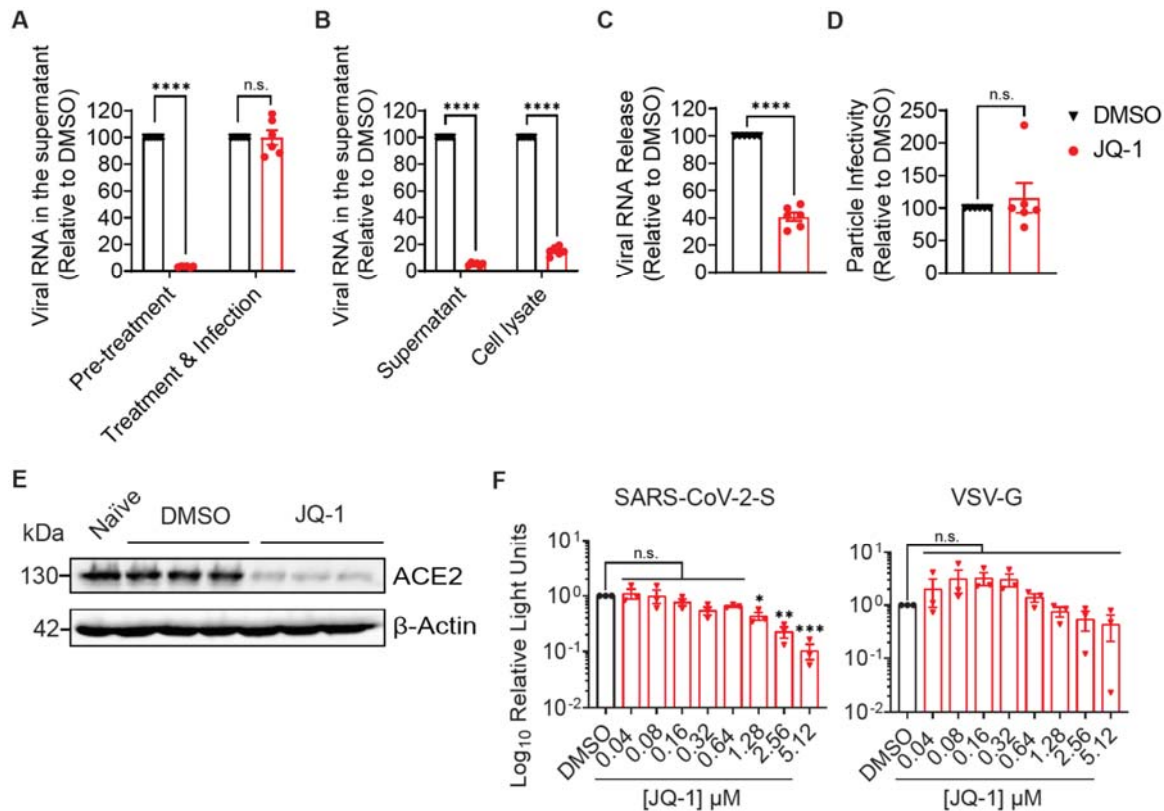
367
368   **Figure 3. JQ-1 exhibits a cell-directed anti-SARS-CoV-2 activity in lung epithelial Calu-3**

369   **cells**

370   (**A**) Calu-3 cells were either pre-treated with JQ-1 (2.56 μM) for 48 hours, followed by SARS-

371   CoV-2 infection (MOI 0.1) and continued treatment (Pre-treatment), or treatment was initiated

372   at the time point of infection (Treatment & Infection). 24 hours post-infection, relative viral

373   RNA abundance in supernatants was quantified.

374   (**B-D**) The relative efficiency of different steps of the replication cycle were quantified
375   following JQ-1 treatment and infection of Calu-3 cells, including (**B**) viral RNA abundance in
376   supernatants and cell lysates, (**C**) particle release and (**D**) specific particle infectivity. The error
377   bars represent the arithmetic mean±SEM from duplicates of three independent experiments.
378   Viral release was calculated by dividing the concentration of viral RNA in the supernatant by
379   the sum of the concentrations of the viral RNA in the supernatant and cell lysate. Particle
380   infectivity was calculated by dividing the viral titers by the corresponding viral RNA
381   concentration in the supernatant.
382   (**E**) Immunoblot analysis of ACE2 expression in JQ-1-treated Calu-3 cells
383   (**F**) Luminometric quantification of transduction efficiency of JQ-1-treated Calu-3 cells using
384   lentiviral pseudoparticles decorated with SARS-CoV-2-S and VSV-G proteins. Error bars
385   represent the mean±SEM from three independent experiments. Unpaired nonparametric
386   Student *t*-test was used to compare the means between the experimental groups.

387   **SARS-CoV-2 infection and JQ-1 treatment modulate the chromatin regulatory landscape**
388   **in lung epithelial Calu-3 cells**
389   To investigate the chromatin regulatory landscape that associates with JQ-1-mediated SARS-
390   CoV-2 inhibition, we subjected Calu-3 cells to bulk ATAC-seq. Principal component analysis
391   (PCA) showed clustering of samples according to their experimental groups, reflecting
392   comparable chromatin profiles between individual samples in each group (Sup. Fig. 2A). JQ-1
393   treatment imposed larger changes than SARS-CoV-2 infection. Samples from uninfected
394   DMSO-treated cells closely clustered with samples from naïve cells, suggesting that DMSO
395   treatment induced minimal changes to the host chromatin profile. Compared to the control
396   groups, JQ-1 administration to Calu-3 cells increased accessibility to the transcriptional start
397   sites (TSS) irrespective of the infection status, followed by SARS-CoV-2 infection, as indicated
398   by the increase in the density of peaks mapping to the TSSs (Fig. 4A), illustrating the
399   differential ability of JQ-1 treatment and SARS-CoV-2 infection to remodel chromatin
400   accessibility to the TSSs. Annotation of the accessible peaks to the genomic features in the
401   chromatin showed a large coverage for promoter sequences located within one kb from the TSS
402   regions across all experimental groups (Fig. 4B). However, irrespective of the infection status,
403   JQ-1 treatment shifted a proportion of the accessible regions away from the promoter
404   sequences located within one kb from the TSS regions to the introns and distal intergenic
405   regions. This suggests that regulation of transcription under JQ-1 treatment is driven by a more
406   evenly-distributed accessibility of genomic features compared to SARS-CoV-2 infection or

407 absence of JQ-1, where transcriptional regulation is predominantly driven by the proximal

408 regulatory cis-elements in the promoters. Hierarchical clustering of significantly regulated

409 peaks in each experimental group revealed distinct chromatin accessibility profiles, modulated

410 distinctly by either SARS-CoV-2 infection or JQ-1 treatment, with some commonly

411 upregulated peaks resulting from both SARS-CoV-2 infection and JQ-1 treatment, respectively

412 (Fig. 4C).

413   Volcano plots of the ATAC-seq data revealed that SARS-CoV-2 infection only mildly

414 modulated the chromatin accessibility profile (significant changes in 130 ATAC-seq peaks, 128

415 of which were accessible while only 2 were inaccessible) (Fig. 4D). In contrast, JQ-1 treatment

416 drastically altered the chromatin accessibility landscape (Fig. 4E, significant changes of 11,434

417 ATAC-seq peaks, 7679 of which were accessible while 3,755 were inaccessible). Strikingly,

418 combination of JQ-1 treatment and infection induced 2.2-fold increased change to the

419 accessibility of genomic regions when compared to JQ-1 treatment only (Fig. 4F, significant

420 changes in 25,306 ATAC-seq peaks, whereby 17,137 were accessible while 8,169 were

421 inaccessible), implying that changes induced by JQ-1 pretreatment are quantitatively superior

422 to those induced by infection.

423   As expected (Wilk et al., 2021; You et al., 2021), compared to uninfected cells,

424 pathways that drive innate immune responses were enriched in the accessible ATAC-seq peaks

425 from SARS-CoV-2-infected cells (Sup. Fig 2B). Accessible ATAC-seq peaks from JQ-1-

426 treated cells showed no significant association with any particular biological pathway when

427 compared to DMSO-treated cells (Sup. Fig 2B-C), suggesting that JQ-1 induced a rather global

428 change rather than alterations of specific biological processes. On the other hand, when

429 compared to infected cells, accessible ATAC-seq peaks from infected cells in the presence of

430 JQ-1 were mostly enriched with ribosome biogenesis and RNA processing pathways (Sup. Fig

431 2B), including RNA splicing reported to be inhibited by SARS-CoV-2 (Banerjee et al., 2020).

432 Of note, nonsense-mediated mRNA decay, a cellular RNA surveillance pathway that exhibits a

433 broad antiviral activity (Balistreri et al., 2014; Wada et al., 2018), was among the highly

434 enriched pathways in the accessible peaks (Sup. Fig 2B). Conversely, pathways associated with

435 sensory perception of smell were downregulated in the accessible peaks from SARS-CoV-2-

436 infected cells, both in the presence of DMSO and JQ-1 (Sup. Fig 2C), but not by JQ-1 *per se*,

437 suggesting an inability of JQ-1 to hamper SARS-CoV-2-mediated downregulation of the smell

438 receptor signalling pathway. Furthermore, accessible peaks from JQ-1-treated infected cells

439 were associated with downregulation of the neuropeptide signalling pathway (Sup. Fig 2C), as

440 opposed to infection or JQ-1 treatment, suggesting JQ-1's potential to interfere with neuronal

441 communication specifically in the infection context. Together, these data show that SARS-

442 CoV-2- and JQ-1-mediated modulation of the chromatin accessibility landscape occurs at

443 multiple levels, with differing magnitudes and breadth.

444   We next searched for transcription factor (TF) binding motifs that were significantly

445 enriched in the accessible ATAC-seq peaks using the DREME algorithm, which is designed to

446 find short and multiple nonredundant binding motifs of eukaryotic TFs and calculate their

447 statistical significance (Bailey, 2011). In infected cells, accessible peaks were enriched for

448 binding motifs for inflammatory TF families, including Signal Transducer and Activator of

449 Transcription (STAT), Interferon Regulatory Factors (IRF) and Nuclear Factor-kappa B

450 (NFkB), which drive IFN signalling and induction of pro-inflammatory cytokines, respectively

451 (Park and Iwasaki, 2020) (Fig. 4G and Sup. Table 1A), suggesting increased accessibility of

452 STAT-, IRF- and NFκB-binding sites to induce IFN response pathways and production of pro-

453 inflammatory cytokines (Bülow Anderberg et al., 2021; Ramasamy and Subbian, 2021). Unlike

454 in SARS-CoV-2 infection, the accessible peaks in JQ-1-treated cells showed significant

455 enrichment of several binding motifs of a wide variety of TF families, suggesting a broader

456 modulation of gene expression by JQ-1 over SARS-CoV-2 infection (Sup. Table 1B-C).

457 Independent of infection, among many others, peaks from JQ-1-treated cells were enriched

458 with binding motifs for TF families such as CNC-bZIP and NF-Y (Fig. 4H-I, Sup. Table 1B-

459 C), which induce antiviral cellular cytoprotective responses (He et al., 2020; Olagnier et al.,

460 2020) and more accessible chromatin (Oldfield et al., 2014, 2019), respectively. Detection of

461 these enrichments, independent of SARS-CoV-2 infection, argues for a dominant role of JQ-1

462 treatment on transcription modulation via the CNC-bZIP and NFY TF families. Secondly,

463 motifs annotated to a superfamily of steroid-induced nuclear receptor (NR) TFs, whose

464 signalling drives cellular RNA splicing processes (Auboeuf et al., 2004; Elhasnaoui et al.,

465 2021), were also enriched in JQ-1-treated groups irrespective of the infection status (Sup. Table

466 1B-C). However, JQ-1 treatment in the presence of SARS-CoV-2 infection (Sup. Table 1C)

467 displayed significant enrichment with TF binding motifs for a wide range of TF families

468 compared to the absence of infection (Sup. Table 1B), suggesting that SARS-CoV-2 infection

469 influences JQ-1-mediated TF profile and likely fine-tunes the JQ-1-mediated transcriptome.

470 Interestingly, compared to uninfected cells, peaks from uninfected JQ-1-treated cells were

471 significantly enriched with a binding motif for NFκB-1/NFκB-2 TFs (Sup. Table 1B), despite

472 JQ-1 being an inhibitor of the NFκB-1-mediated canonical pathway that induces cytokine

473 production (Samelson et al., 2022). Together, these data illustrate the genome-wide TF binding

474   profiles that drive the transcriptional programs governing SARS-CoV-2 infection- and JQ-1-

475   mediated changes.
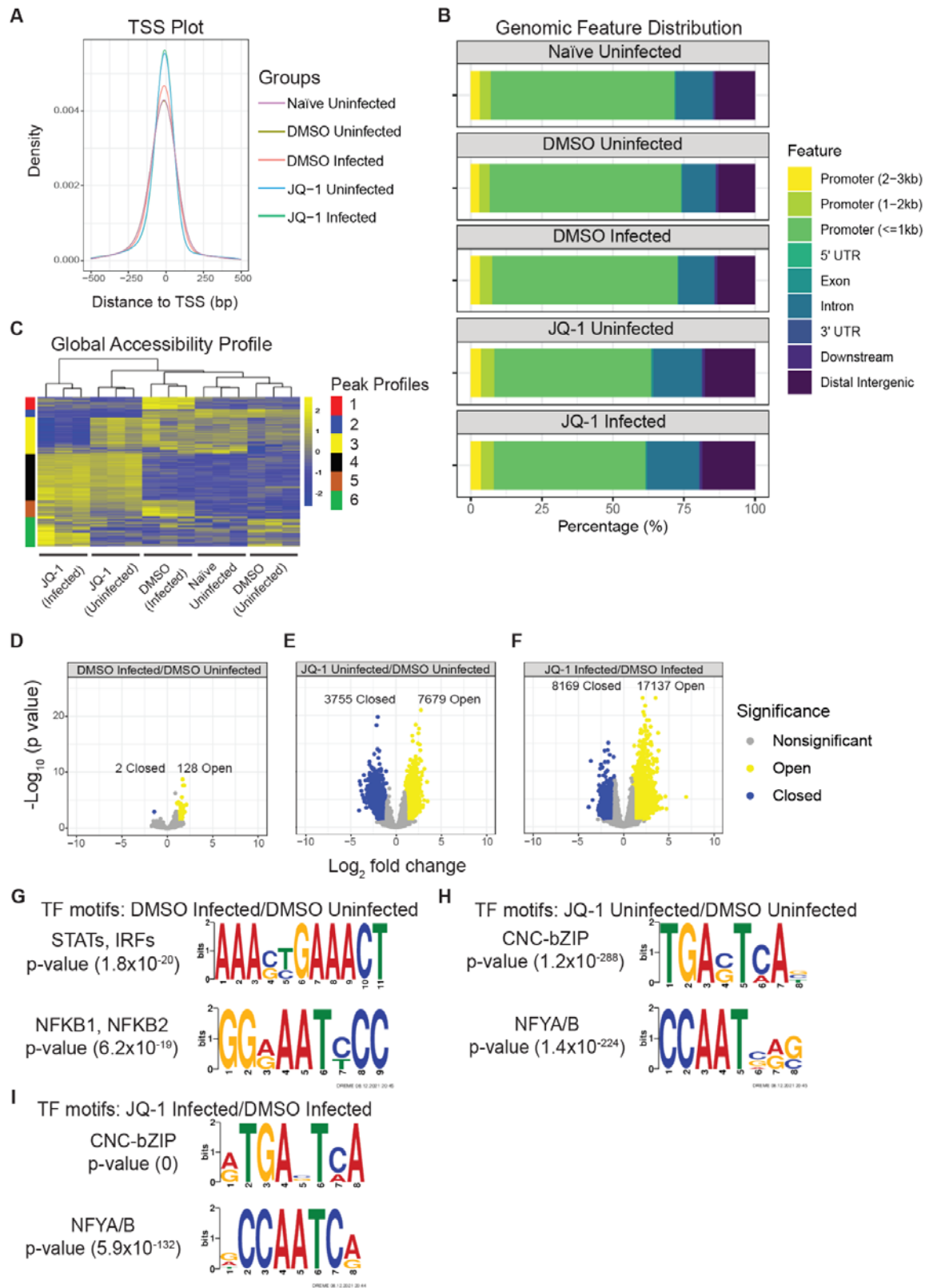
Figure 4. SARS-CoV-2 infection and JQ-1 treatment modulate the chromatin regulatory landscape in lung epithelial Calu-3 cells.

479　(**A**) TSS plot depicting the density and distribution of accessible ATAC-seq peaks around

480　transcription start sites within a window of -500 to 500 bp.

481　(**B**) Analysis of the genomic features annotated to accessible ATAC-seq peaks in the

482　chromatin. (**C**) Heatmap hierarchical clustering of differentially accessible ATAC-seq peaks

483　scaled as z-score across rows.

484　Volcano plots showing relative $\log_2$FC and statistical significance of differentially regulated

485　ATAC-seq peaks in (**D**) DMSO-treated infected versus DMSO-treated uninfected, (**E**) JQ-1-

486　treated uninfected versus DMSO-treated, uninfected and (**F**) JQ-1-treated infected versus

487　DMSO-treated, infected contrasts. Significantly (FDR of ≤0.05) regulated peaks are indicated.

488　TF motif enrichment analysis from the accessible ATAC-seq peaks in (**G**) DMSO-treated,

489　infected versus DMSO-treated uninfected, (**H**) JQ-1-treated uninfected versus DMSO-treated,

490　uninfected and (**I**) JQ-1-treated infected versus DMSO-treated, infected contrasts. The TF

491　motifs were identified using the DREME algorithm, where the height of the letters represents

492　the frequency of each base in the motif.

493　**SARS-CoV-2- and JQ-1-mediated modulations of the chromatin accessibility landscape**

494　**underlie the transcriptomic and proteomic changes in lung epithelial Calu-3 cells**

495　Next, we subjected the samples to bulk RNA-seq and mass spectrometry to establish their

496　transcriptomic and proteomic profiles, respectively, including the downstream effects of SARS-

497　CoV-2- and JQ-1-mediated modulations on the chromatin accessibility landscape. PCA of the

498　RNA-seq data revealed that the samples clustered according to their experimental groups,

499　reflecting similar transcriptomic profiles between replicates in each group (Sup. Fig. 3A). As in

500　ATAC-seq (Sup. Fig. 2A), JQ-1 treatment induced more important changes than SARS-CoV-2

501　infection. Samples from naïve and uninfected DMSO-treated cells clustered close to each other,

502　with minimal effect of DMSO treatment on the cellular transcriptome (Sup. Fig. 3A).

503　SARS-CoV-2 infection induced significant changes to the expression of 6866 genes, of

504　which 3323 were upregulated and 3543 downregulated (Fig. 5A). In the absence of infection,

505　JQ-1 treatment induced significant changes to the expression of 10,778 genes, of which 5285

506　were upregulated and 5493 were downregulated (Fig. 5B). On the other hand, when compared

507　to infection only, JQ-1 treatment of infected cells induced significant changes to the expression

508　of 11,195 genes, with 5128 upregulated and 6067 downregulated (Fig. 5C). Again, these data

509　suggest that JQ-1 treatment modulates the host transcriptome to a larger extent compared to

510　SARS-CoV-2 infection.

511 Hierarchical clustering of genes driving selected biological pathways revealed that

512 SARS-CoV-2 infection induced upregulation of IFN-stimulated genes (Fig. 5D). JQ-1-treated

513 groups, irrespective of their infection status, shared similar transcriptomic signatures for the

514 displayed pathways, as did the uninfected DMSO-treated and naïve groups. Compared to other

515 groups, JQ-1 treatment altered the cell cycle transcriptomic profile and upregulated genes

516 driving autophagy and NRF-2-mediated cellular cytoprotective response, irrespective of the

517 infection status (Fig. 5D). As expected, IFN and cytokine-mediated signalling pathways were

518 upregulated in SARS-CoV-2-infected samples, while pathways driving oxidative

519 phosphorylation were among the top downregulated pathways (Sup. Fig. 3B). Conversely, JQ-1

520 treatment in the presence of infection upregulated the pathways driving oxidative

521 phosphorylation and downregulated the IFN and cytokine signalling pathways (Sup. Fig. 3B).

522 These JQ-1-driven changes were less pronounced or even absent in the absence of infection

523 (Sup. Fig. 3B). Nucleosome assembly, organisation, chromatin assembly, and other pathways

524 associated with regulation of gene transcription were equally enriched across all analysed

525 contrasts (Sup. Fig. 3B).

526 To generate proteomic profiles, we resolved proteins from the whole cell lysate on

527 linear SDS-PAGE gels, visualised the proteins with Bio-Safe Coomassie Blue stain (Sup. Fig.

528 3C) and subjected them to liquid chromatography coupled with tandem mass spectrometry

529 (LC-MS/MS) as described elsewhere (Mhlekude et al., 2021). PCA from the proteomic data

530 demonstrated sample clustering according to their experimental groups, reflecting similar

531 proteomic profiles between individual samples in each group (Sup. Fig. 3D). SARS-CoV-2

532 infection induced differential abundance of 71 proteins, with 33 upregulated and 38

533 downregulated (Fig. 5E). In the absence of infection, JQ-1 treatment induced differential

534 regulation of 761 proteins, 189 of which were upregulated and 563 downregulated (Fig. 5F).

535 JQ-1 treatment in the presence of SARS-CoV-2 infection induced differential regulation of 476

536 proteins, with 187 upregulated and 289 downregulated (Fig. 5G).

537 GO term analysis of the biological processes revealed that IFN and innate immune

538 signalling driven by the STATs, IRFs, and NF-κB-1 transcription factors were among the

539 upregulated pathways in SARS-CoV-2-infected samples, as compared to uninfected samples

540 (Fig. 5H). Furthermore, chromatin silencing and nucleosome assembly were the top two

541 highly-enriched pathways. Irrespective of the infection status, IFN signalling, chromatin

542 silencing, nucleosome assembly, and G1/S transition of cell cycle were among the

543 downregulated pathways in JQ-1-treated groups (Fig. 5 I-K). Paradoxically, nucleosome

544 assembly and chromatin organisation-related pathways were upregulated at the transcriptomic

545   levels between the JQ-1-treated groups irrespective of the infection status (Sup. Fig. 5B), but

546   downregulated at the proteomic level (Fig. 5I-K). On the other hand, irrespective of the

547   infection status, the NRF-2-driven oxidant detoxification pathway that forms part of the cellular

548   antiviral cytoprotective response was among the upregulated pathways in the JQ-1-treated

549   groups (Fig. 5J-L). Moreover, the autophagy pathway, which is reduced by SARS-CoV-2

550   (Gassen et al., 2021), was upregulated in the JQ-1-treated group in the presence of infection

551   (Fig. 5L). Together, the transcriptomic and proteomic changes largely recapitulate the

552   modulated biological pathways, which are driven by transcription factors whose binding motifs

553   are enriched as determined by ATAC-seq.
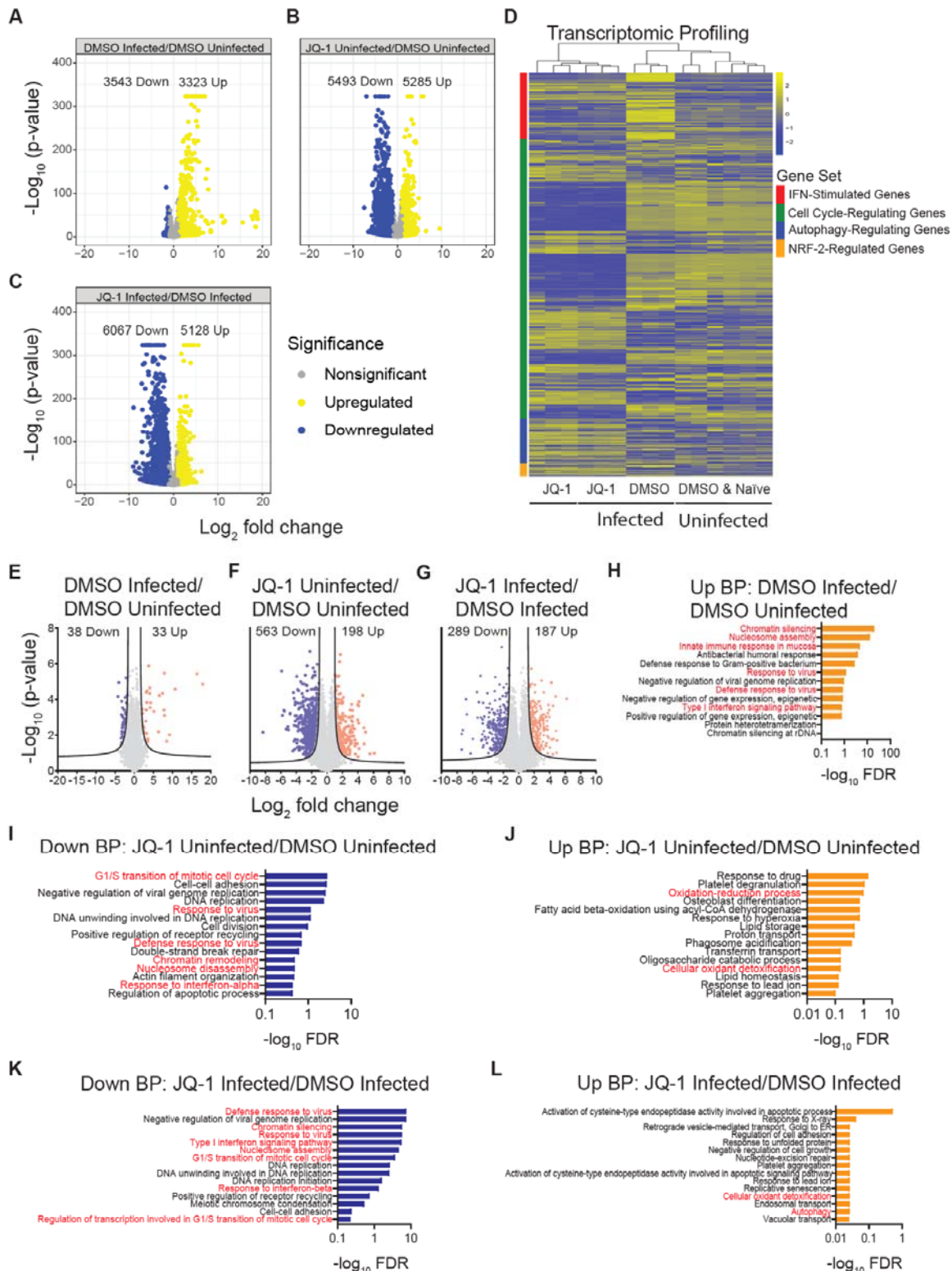
Figure 5. SARS-CoV-2 infection- and JQ-1-mediated modulations of the chromatin accessibility landscape underlie the transcriptomic and proteomic profiles in lung epithelial Calu-3 cells.

558 Volcano plots showing relative $\log_2$FC and statistical significance of differentially expressed
559 genes in (**A**) DMSO-treated infected versus DMSO-treated uninfected, (**B**) JQ-1-treated
560 infected versus DMSO-treated infected and (**C**) JQ-1-treated uninfected versus DMSO-treated
561 uninfected contrasts. The number of significant (FDR of ≤0.05) DRGs are indicated.

562 (**D**) Heatmap of DRGs across four biological pathways (IFN-stimulated genes, cell cycle-
563 regulating genes, autophagy-regulating genes, and NRF-2-regulated genes) scaled as z-score
564 across rows.

565 Volcano plots showing relative $\log_2$FC and statistical significance of differentially abundant
566 proteins in (**E**) DMSO-treated infected versus DMSO-treated uninfected, (**F**) JQ-1-treated
567 uninfected versus DMSO-treated uninfected and (**G**) JQ-1-treated infected versus DMSO-
568 treated, infected contrasts. The number of significantly (FDR ≤0.05) regulated proteins is
569 indicated.

570 Top enriched (FDR ≤0.05) GO Biological Process terms of upregulated proteins in (**H**) DMSO-
571 treated infected versus DMSO-treated, uninfected, and differentially regulated proteins in (**I-J**)
572 JQ-1-treated, infected versus DMSO-treated infected and (**K-L**) JQ-1-treated uninfected versus
573 DMSO-treated uninfected contrasts.

574 **JQ-1 treatment antagonises SARS-CoV-2-mediated suppression of the antiviral NRF-2-**
575 **mediated cytoprotective response**

576 Despite the growing literature on the anti-SARS-CoV-2 activity of JQ-1 and other iBETs
577 (Gilham et al., 2021; Mills et al., 2021; Samelson et al., 2022; Vann et al., 2022), TFs
578 orchestrating transcriptional responses in the context of JQ-1-mediated anti-SARS-CoV-2
579 activity remain to be investigated. For this purpose, we performed global TF activity profiling
580 using the bulk RNA-seq dataset, which was collected in parallel with ATAC-seq data to
581 identify TFs with significantly regulated gene module scores across our experimental groups.
582 SARS-CoV-2 infection of Calu-3 cells induced activity of the inflammatory TF families
583 (STATs, IRFs, and NFκB-1) (Fig. 6A), whose signalling is associated with severe COVID-19
584 cases (Lam et al., 2021). JQ-1 treatment in the presence of SARS-CoV-2 infection suppressed
585 the activity of these inflammatory TF families, suggesting an anti-inflammatory effect of JQ-1
586 (Fig. 6A). Interestingly, while SARS-CoV-2 infection induced NFκB-1-driven canonical
587 signalling pathway, it strongly suppressed NFκB-2-driven noncanonical signalling pathway,
588 reflecting a more precise SARS-CoV-2-mediated regulation of NFκB signalling pathways.

589   Irrespective of the infection status, JQ-1 treatment suppressed activity of the TF
590 families that regulate cell cycle and proliferation (E2F & MYB), whose synergistic signalling is

591 associated with severe lung injury in COVID-19 cases (Lam et al., 2021). This is in line with
592 JQ-1-mediated dysregulation of cell cycle-regulating genes (Fig. 5D) and downregulation of
593 pathways driving G1/S transition of the mitotic cell cycle captured in the proteomic data in
594 (Figs. 5 I-K). Furthermore, JQ-1 also induced the transcriptional activities of nuclear factor
595 (erythroid-derived-2)-like-2 (NFL2L2)/(NRF-2) and androgen receptor (AR), which drive a
596 cytoprotective response (He et al., 2020) and RNA alternative splicing (Rana et al., 2021; Shah
597 et al., 2020), respectively (Fig. 6A). It is noteworthy that pharmacological induction of NRF-2
598 signalling by 4-OI and DMF inhibits SARS-CoV-2 replication *in vitro* (Olagnier et al., 2020).
599 NRF-2 and AR belong to CNC-bZIP and steroid nuclear receptor (NR) families of TFs,
600 respectively; whose binding motifs were significantly enriched in the accessible ATAC-seq
601 peaks from JQ-1-treated cells independent of the infection status (Sup. Table 1B-C). Together,
602 these data suggest that the chromatin regulatory regions captured in our ATAC-seq data were
603 not only accessible, but also transcriptionally active.

604 To discern between SARS-CoV-2-mediated upregulation of IFN signalling, inhibition
605 of NRF-2 signalling, and JQ-1-mediated antagonistic effects in these processes, we generated
606 volcano plots to analyse the $\log_2$FCs of STAT/IRF and NRF-2 target genes. As expected, IFN-
607 stimulated genes (ISGs) were upregulated in the context of SARS-CoV-2 infection (Fig. 6B).
608 SARS-CoV-2 infection showed minimal changes on the expression of NRF-2 target genes and
609 no effect on NRF-2 expression *per se* (Fig. 6B). JQ-1 treatment induced the downregulation of
610 ISGs in the absence (Fig. 6C) and presence (Fig. 6D) of SARS-CoV-2 infection. Irrespective of
611 the infection status, JQ-1 treatment induced an upregulation of the expression of NRF-2 target
612 genes (Fig. 6C-D). Like SARS-CoV-2 infection (Fig. 6B), JQ-1 treatment did not significantly
613 change expression of NRF-2 itself, independent of the infection status (Fig. 6C-D). These data
614 suggest that both SARS-CoV-2 and JQ-1-mediated modulations of NRF-2 signalling do not
615 significantly alter NRF-2 expression *per se*, but likely modulate the expression of its signalling
616 cofactors.

617 NRF-2 induces gene expression by binding to the *cis*-acting antioxidant response
618 elements (ARE) on the promoters of its target genes as a heterodimer with the small
619 musculoaponeurotic fibrosarcoma (MAF) transcription factors, which act as its indispensable
620 cofactors (Itoh et al., 1997; Katsuoka and Yamamoto, 2016). Furthermore, transmembrane B
621 cell lymphoma 2-associated X protein (BAX) inhibitor motif-containing 6 (TMBIM6) protects
622 the host against oxidative stress by inducing NRF-2 signalling (Kim et al., 2020; Lee et al.,
623 2007). Interestingly, the proteomic data showed significant reduction of $\log_2$FCs for MAFK
624 and TMIBM6, and NRF-2 target proteins in SARS-CoV-2-infected Calu-3 cells (Fig. 6E). JQ-1

625   treatment antagonised these SARS-CoV-2-mediated changes, with more pronounced inhibition

626   in the context of infection (Fig. 6E). These data suggest that SARS-CoV-2 suppresses NRF-2

627   signalling by downregulating its indispensable signalling cofactors.

628   Further log$_2$FC analysis revealed that SARS-CoV-2 infection induced a dramatic

629   upregulation of COQ6 expression (Sup. Fig. 4A), which drives the production of coenzyme

630   Q10 to shuttle electrons between complexes I, II and II; and associated dehydrogenase enzymes

631   in the mitochondrial electron transport chain (Acosta Lopez et al., 2019; Wang and Hekimi,

632   2016). These data hint at the need for a ubiquinone biosynthetic pathway in SARS-CoV-2

633   pathogenesis, despite the defective oxidative phosphorylation (Sup. Fig. 3B). Moreover, SARS-

634   CoV-2 infection downregulated COX16 that serves as an indispensable component of

635   cytochrome-c-oxidase (complex IV) in the electron transport chain (Wintjes et al., 2021) and

636   upregulated the chromatin silencing histone variants (H2AFY, H2AFV and H2AFZ) (Sup. Fig.

637   4A), which likely drive the SARS-CoV-2-mediated upregulation of chromatin silencing and

638   nucleosome assembly pathways (Fig. 5H). More importantly, SARS-CoV-2 downregulated the

639   expression of YTHDF2, a methyl-6-adenosine (m6A) reader of the RNA molecules in the host

640   that binds to and degrade m6A-bearing host (Du et al., 2016) and viral (Gokhale et al., 2016;

641   Gonzales-van Horn and Sarnow, 2017; Lichinchi et al., 2016) RNA molecules to prevent the

642   expression of aberrant cellular RNA and inhibit viral replication, respectively. JQ-1 displayed

643   an antagonistic effect against the above-mentioned SARS-CoV-2-mediated proteomic

644   modulations (Sup. Fig. 4A).

645   NRF-2 signalling, which is induced by JQ-1 treatment in Calu-3 cells (Fig. 6A), inhibits

646   SARS-CoV-2 infection when induced by 4-OI and DMF (Olagnier et al., 2020). This prompted

647   us to investigate whether pharmacological inhibition of NRF-2 signalling antagonises JQ-1-

648   mediated anti-SARS-CoV-2 activity. Interestingly, co-treating Calu-3 cells with JQ-1 and

649   ML385, a specific inhibitor of NRF-2 (Singh et al., 2016), prior to infection, led to a significant

650   increase in viral RNA copies (Fig. 6F) and infectious titers (Fig. 6G-H) in the supernatant

651   compared to JQ-1 and DMSO co-treated cells, in the absence of detectable cell toxicity (Fig.

652   7I). These data suggest that JQ-1 inhibition of SARS-CoV-2 infection in Calu-3 cells involves

653   efficient NRF-2 signalling. Together, these data shed light on JQ-1-mediated multi-pronged

654   approach underlying its anti-SARS-CoV-2 activity.
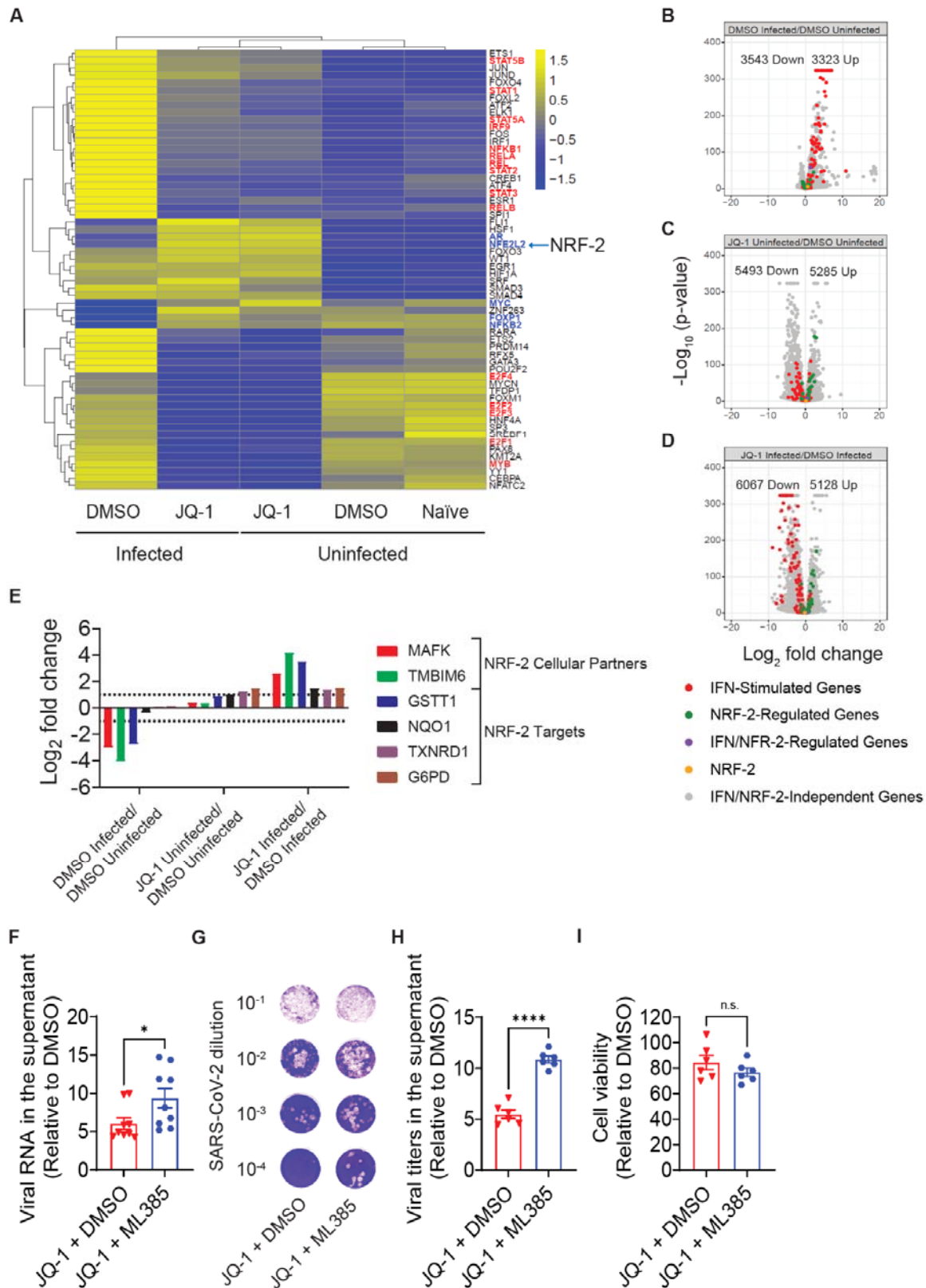
Figure 6. JQ-1 treatment antagonises SARS-CoV-2-mediated suppression of the antiviral NRF-2-mediated cytoprotective response

658   (**A**) Scaled TF activity scores in different treatments for RNAseq data, based on the Dorothea

659   database.

660   Volcano plots showing relative $\log_2$FC and statistical significance of differentially expressed

661   genes involved in IFN and NRF-2 signalling in (**B**) DMSO-treated infected versus DMSO-

662   treated uninfected, (**C**) JQ-1-treated infected versus DMSO-treated infected and (**D**) JQ-1-

663   treated uninfected versus DMSO-treated uninfected contrasts.

664   (**E**) $\log_2$FC analysis of differentially expressed proteins implicated in NRF-2 signalling. The

665   bars indicate relative $\log_2$FC in expression between indicated contrasts and proteins with a

666   relative $\log_2$FC of >1 and a FDR≤0.05 were considered significant.

667   Relative quantification of (**F**) viral RNA copies and (**G-H**) infectivity from SARS-CoV-2

668   infected Calu-3 cells treated as indicated. The data were expressed as the normalised

669   percentage infection relative to DMSO only-treated cells. Error bars show the SEM from

670   triplicates of three and two independent experiments respectively.

671   (**I**) Cell viability analysis in Calu-3 cells treated as indicated. The graphs show background-

672   subtracted and normalised data relative to DMSO only-treated cells. Error bars show the SEM

673   from triplicates of two independent experiments.

674   Unpaired nonparametric Student *t*-test was used to compare the means between experimental
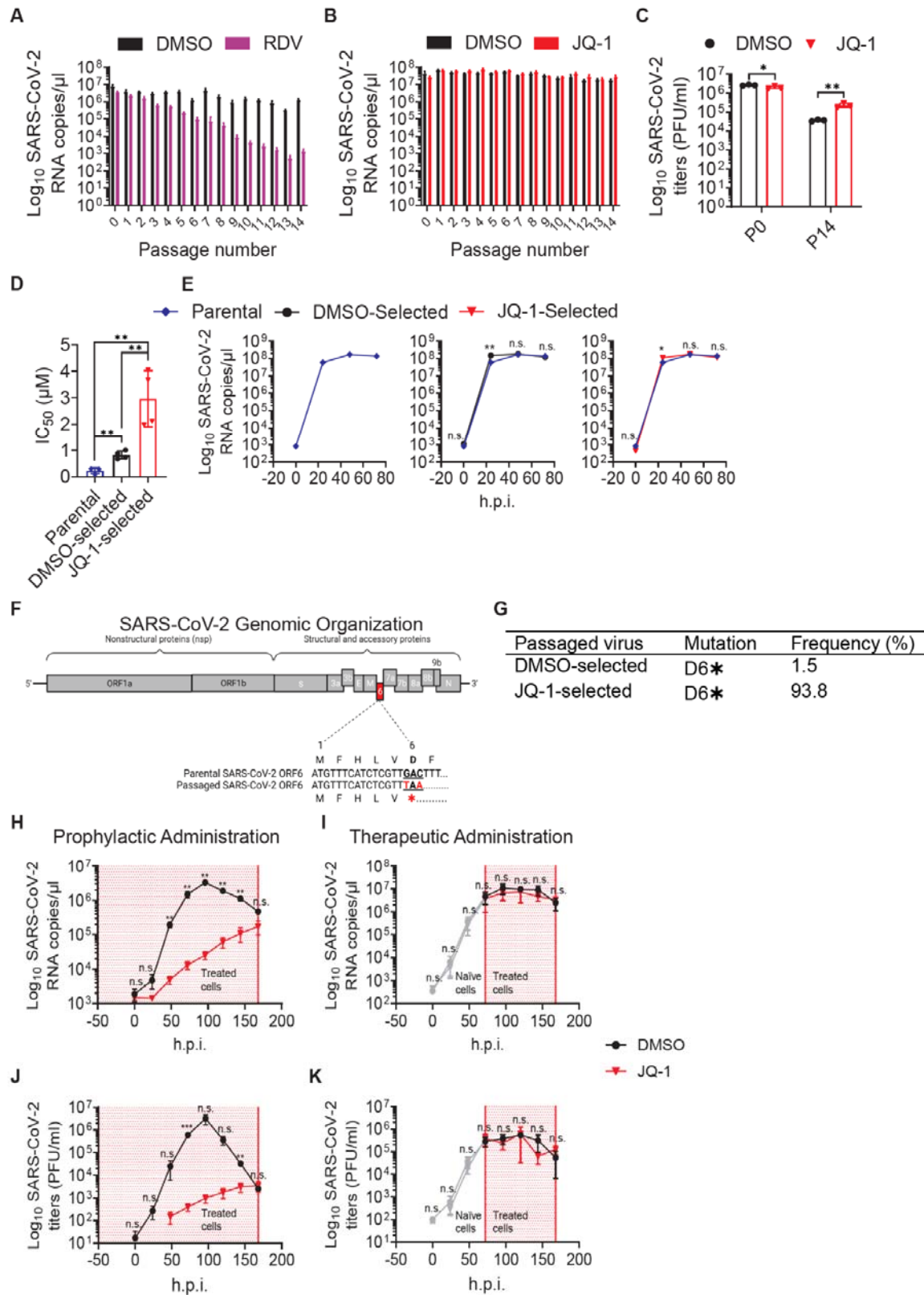
675   groups.

SARS-CoV-2 subverts JQ-1-mediated antiviral state in lung epithelial Calu-3 and human

bronchial airway epithelial cells

678   SARS-CoV-2 can adapt to and acquire resistance against potent virus-directed antivirals such

679   as remdesivir (RDV) *in vitro* (Stevens et al., 2022; Szemiel et al., 2021), a replication

680   bottleneck that induces the emergence SARS-CoV-2 variants *in vivo* (Heyer et al., 2022). To

681   investigate whether SARS-CoV-2 can acquire resistance to iBETs, we serially passaged it in

682   Calu-3 cells under escalating two-fold concentrations of JQ-1 (Sup. Fig. 5A), along with RDV

683   as a reference. SARS-CoV-2 serial passaging under increasing two-fold concentrations of RDV

684   led to a gradual reduction of viral RNA copies in the supernatant, with a potential resistance

685   phenotype emerging at the earliest at passage 14 (Fig. 7A). In contrast, SARS-CoV-2 serial

686   passaging under escalating two-fold concentrations of JQ-1 displayed unrelenting high

687   concentrations of viral RNA copies from passage two until passage 14. These data suggest a

688   transient nature of JQ-1-mediated anti-SARS-CoV-2 activity and early adaptation of SARS-

689   CoV-2 to JQ-1 (Fig. 7B). Quantification of viral titers from passages one and 14 revealed that

690   SARS-CoV-2 virions were sensitive to JQ-1 treatment at the beginning of the passaging

691 experiments, and acquired resistance and replication fitness to JQ-1 during serial passaging
692 (Fig. 7C).

693   To determine the extent to which SARS-CoV-2 passaging under JQ-1 led to the
694 acquisition of resistance, we investigated the sensitivity of DMSO- and JQ-1-selected SARS-
695 CoV-2 virions to JQ-1 in Calu-3 cells by quantifying the viral RNA copies in the supernatant
696 and calculating IC_{50} concentrations. Compared to parental SARS-CoV-2, virions that were
697 serially passaged under JQ-1 exhibited reduced sensitivity to JQ-1 treatment in Calu-3 cells
698 (Fig. 7D), which was more pronounced (12-fold) compared to DMSO-selected virions (4-fold)
699 (Sup. Fig. 5B). Viral growth kinetics in Calu-3 cells showed that DMSO- and JQ-1-selected
700 SARS-CoV-2 virions may have acquired some degree of replication fitness compared to the
701 parental SARS-CoV-2 virions (Fig. 7E). Next-Generation Sequencing (NGS) revealed virus
702 sequences encoding a premature stop codon at position six of ORF6 in the genome from virions
703 passagaged in the presence of JQ-1, as opposed to parental virus (Fig. 7F). This premature stop
704 codon was present far more frequently in JQ-1-selected virions (93.8% of reads covering this
705 region) than DMSO-selected virions (1.5% of reads covering this region) (Fig. 7G).

706   Finally, we performed kinetic, multi-cycle infection experiments in hBAECs to
707 compare JQ-1-mediated anti-SARS-CoV-2 activity in the contexts of prophylactic and
708 therapeutic treatment. In the set-up mimicking prophylactic administration, we started
709 treatment of hBAECs with DMSO or JQ-1 48 hours prior to SARS-CoV-2 infection (Sup. Fig.
710 5C). For therapeutic administration, we infected naïve hBAECs and started treatment 48 hours
711 post-infection (Sup. Fig. 5D). JQ-1 treatment was continued for the duration of the entire
712 experiment. Prophylactic administration of JQ-1 resulted in antiviral activity that was more
713 pronounced earlier post infection, which however vanished over time, as indicated by the
714 gradual increase in viral RNA copies (Fig. 7H) and infectious titers (Fig. 7J). Strikingly,
715 administration of JQ-1 post establishment of infection failed to curb SARS-CoV-2 replication,
716 as indicated by similar viral RNA copies (Fig. 7I) and infectious titers (Fig. 7I) between
717 DMSO- and JQ-1-treated groups. Together, these data suggest that JQ-1 treatment results in a
718 transient antiviral state, which however can be subverted by SARS-CoV-2.

719
720 **Figure 7. SARS-CoV-2 infection subverts JQ-1-mediated antiviral state in lung epithelial**

721 **Calu-3 and human bronchial airway epithelial cells (hBAECs).**

722   Quantification of SARS-CoV-2 RNA (copies/µl) from triplicates of 15 serial passages under

723   two-fold escalating concentrations of (**A**) remdesivir and (**B**) JQ-1, with DMSO as a mock.

724   (**C**) Quantification of SARS-CoV-2 titers (PFU/ml) in triplicates from P1 (JQ-1 0.32µM) and

725   P14 (JQ-1 5.12µM) passages. The means between experimental groups were compared using

726   nonparametric Student *t*-test.

727   (**D**) Quantification of IC_{50} values from JQ-1 dose-dependent inhibition curves determined in

728   JQ-1-treated Calu-3 cells infected with parental and passaged SARS-CoV-2 virions (MOI 0.1).

729   The error bars represent the mean±SEM from four independent experiments and the means

730   between experimental groups were compared using nonparametric Student *t*-test.

731   (**E**) Viral growth kinetics in DMSO-treated Calu-3 cells showing viral RNA quantities from

732   parental and passaged (P14) SARS-CoV-2 virions (MOI 0.1) from three independent

733   experiments. The means between experimental groups were compared using nonparametric

734   multiple *t*-test.

735   (**F**) Schematic diagram of the SARS-CoV-2 genome depicting the mutation creating a

736   premature stop codon at position six of ORF6 among the passaged (P14) virions.

737   (**G**) Quantification of the ORF6 D6✱ mutation frequency from sequences from

738   passaged (P14) SARS-CoV-2 virions.

739   Virus growth kinetics in DMSO and JQ-1 (2.56 µM)-treated hBAECs depicting SARS-CoV-2

740   RNA quantities (copies/µl) in the contexts of (**H**) prophylactic and (**I**) therapeutic drug

741   administration from three independent experiments.

742   Virus growth kinetics in DMSO and JQ-1 (2.56 µM)-treated hBAECs depicting SARS-CoV-2

743   titers (PFU/ml) in the contexts of (**J**) prophylactic and (**K**) therapeutic drug administration from

744   three independent experiments.

745   The area shaded in red indicates the time period of drug administration and the grey lines in the

746   context of therapeutic administration indicate infection before drug administration. The means

747   between experimental groups were compared using nonparametric multiple *t*-test. Error bars

748   represent the mean±SEM.

749   **DISCUSSION**

750   Prior studies attributed the iBET-mediated anti-SARS-CoV-2 activity to the

751   downregulation of cellular ACE2 expression (Gilham et al., 2021; Mills et al., 2021; Samelson

752   et al., 2022), but failed to capture the pleiotropic nature of the antiviral state induced by these

753 compounds and their susceptibility to SARS-CoV-2 subversion. Here, we show that JQ-1-
754 mediated anti-SARS-CoV-2 activity goes beyond the downregulation of ACE2 expression by
755 inducing a vast transcriptional remodulation, including the mounting of antiviral NRF-2-
756 mediated responses. Furthermore, we show that JQ-1-mediated antiviral activity is transient
757 when administered prophylactically and nullified by SARS-CoV-2 when administered
758 therapeutically following an established infection, suggesting effective viral antagonistic
759 strategies.

760 In agreement with prior studies in Calu-3 cells (Gilham et al., 2021; Mills et al., 2021;
761 Samelson et al., 2022; Vann et al., 2022), iBETs displayed an antiviral activity against SARS-
762 CoV-2 infection in lung epithelial Calu-3 cells and hBAECs when administered
763 prophylactically, suggesting that the iBET-mediated anti-SARS-CoV-2 activity is readily
764 translated from cell lines *in vitro* to clinically relevant human-derived infection models. The
765 antiviral activity of JQ-1 and its analogues has largely been reported in the context of SARS-
766 CoV-2 parental strains (Gilham et al., 2021; Mills et al., 2021; Samelson et al., 2022) and VOC
767 Delta (Vann et al., 2022). Our data showing sensitivity of SARS-CoV-2 and SARS-CoV, but
768 not MERS-CoV, to JQ-1 suggest that MERS-CoV replication, and likely that of other
769 *Merbecoviruses*, is independent of BET proteins. This difference can potentially be attributed
770 to the interactions between SARS-CoV-2-E and cellular BET proteins (Chen et al., 2022; Vann
771 et al., 2022), through a conserved histone motif present in SARS-CoV-E and SARS-CoV-2-E
772 proteins (Gordon et al., 2020; Schoeman and Fielding, 2020), which is lacking in MERS-CoV-
773 E protein (Schoeman and Fielding, 2020).

774 The regulatory landscape orchestrating the iBET-mediated transcriptional responses to
775 SARS-CoV-2 infection has remained largely unexplored. Accessible peaks in SARS-CoV-2-
776 infected samples were enriched with binding motifs for the inflammatory TF family (STATs,
777 IRFs and NFκB), which were significantly associated with the upregulation of IFN and
778 cytokine signalling pathways. On the other hand, accessible peaks from the same samples were
779 significantly associated with the downregulation of smell receptor signalling pathways,
780 reminiscent of the olfactory dysfunction reported in COVID-19 cases (Brann et al., 2020; de
781 Melo et al., 2021; Qiu et al., 2020). Significant association of accessible peaks from JQ-1-
782 treated samples in the presence of infection with the downregulation of the smell receptor
783 signalling pathways suggests that JQ-1 is unable to dampen SARS-CoV-2-mediated olfactory
784 dysfunction (Brann et al., 2020; de Melo et al., 2021; Qiu et al., 2020).

785 Similar to the ATAC-seq data , we captured massive differential regulation of genes and
786 proteins in JQ-1-treated samples, irrespective of infection, compared to SARS-CoV-2 infection.

787   Upregulated genes and proteins in SARS-CoV-2-infected samples were significantly associated

788   with the upregulation of IFN and cytokine signalling pathways. In line with the detected

789   enrichment of accessible binding motifs for the inflammatory TF family, supervised

790   hierarchical clustering further showed that SARS-CoV-2 infection induced the transcription of

791   IFN-stimulated genes. In accordance with reported SARS-CoV-2-mediated impairment of

792   mitochondrial biogenesis (Guarnieri et al., 2022), downregulated genes in SARS-CoV-2-

793   infected samples were significantly associated (among others) with the downregulation of

794   pathways driving mitochondrial oxidative phosphorylation (OXPHOS). The upregulation of

795   chromatin silencing and nucleosome assembly pathways at the proteomic level in SARS-CoV-

796   2-infected samples is consistent with SARS-CoV-2-ORF8-mediated chromatin compaction

797   (Kee et al., 2021) and may represent the epigenomic mechanism underlying SARS-CoV-2-

798   mediated host-shutoff (Finkel et al., 2021).

799   Interestingly, despite inducing a strong NFκB-1 TF activity that drives inflammatory

800   cytokine production (Ramasamy and Subbian, 2021), SARS-CoV-2 infection induced an

801   equally strong suppression of NFκB-2 TF activity, which regulates the maturation of antibody-

802   producing B cells and development of germinal centres (GC) in the lymph nodes (Caamaño et

803   al., 1998; Silva et al., 2016). Conversely, irrespective of infection, JQ-1 suppressed NFκB-1 TF

804   activity and induced NFκB-2 TF activity. It is noteworthy that inhibition of NFκB-1

805   transcriptional footprint inhibits SARS-CoV-2 replication (Nilsson-Payant et al., 2021). These

806   data reflect a carefully executed and precise regulation of NFκB-mediated signalling pathways

807   by SARS-CoV-2 infection and JQ-1 administration.

808   Association of the upregulated genes and proteins in JQ-1-treated samples with the

809   downregulation of IFN signalling and viral genome replication pathways validates JQ-1-

810   mediated suppression of innate immune responses (Chen et al., 2022; Mills et al., 2021;

811   Samelson et al., 2022) and antiviral activity (Gilham et al., 2021; Mills et al., 2021; Samelson

812   et al., 2022; Vann et al., 2022). SARS-CoV-2 infection limits induction of autophagy (Gassen

813   et al., 2021), and pharmacological induction of NRF-2, which is a cellular cytoprotective

814   response-inducing transcription factor that belongs to CNC-bZIP TF family, inhibits SARS-

815   CoV-2 replication (Olagnier et al., 2020). Of note, a binding motif for CNC-bZIP TF family

816   was among the top enriched TF motifs in accessible peaks from JQ-1-treated samples,

817   irrespective of infection.

818   Of particular interest, supervised hierarchical clustering revealed that JQ-1 treatment

819   upregulated the expression of autophagy-regulating and NRF-2 target genes, irrespective of

820   SARS-CoV-2 infection. In accordance, pathway enrichment analysis at the proteomic level

821   revealed upregulation of autophagy in JQ-1-treated samples in the presence of infection and

822   NRF-2-mediated cellular oxidant detoxification pathway irrespective of infection status. Motif

823   enrichment for the TFs belonging to CNC-bZIP and NFY families in the context of JQ-1

824   administration, irrespective of infection, revealed the chromatin regulatory landscape

825   underlying JQ-1-mediated induction of NRF-2 signalling (Lv et al., 2022), which exhibits an

826   anti-SARS-CoV-2 activity in the context of DMF- and 4-OI-mediated induction (Olagnier et

827   al., 2020). Moreover, signalling by the NFY TFs increases chromatin accessibility by

828   preventing nucleosome encroachment (Oldfield et al., 2014, 2019). Therefore, enrichment of

829   the binding motifs for the NFY TFs supports the highly accessible chromatin landscape

830   detected in the context of JQ-1 treatment. Together, these data show that JQ-1 induced the

831   activities of NRF-2, which drive the induction of antiviral cellular cytoprotective response

832   (Olagnier et al., 2020).

833   SARS-CoV-2 infection upregulated IFN-stimulated genes, but displayed minimal

834   alterations on the expression of NRF-2 target genes, without altering NRF-2 expression *per se*.

835   On the other hand, JQ-1 administration downregulated the expression of IFN-stimulated genes

836   and induced the expression of NRF-2 target genes irrespective of infection. However, like

837   SARS-CoV-2 infection, JQ-1 administration also did not alter NRF-2 expression, despite

838   significantly altering the expression of its target genes. These data suggest that differential

839   regulation of NRF-2 signalling by SARS-CoV-2 infection and JQ-1 administration does not

840   alter NRF-2 expression *per se*, but likely the expression of its signalling co-factors.

841   Accordingly, the proteomic data showed that SARS-CoV-2 infection induced

842   significant log_2FC downregulation of MAFK and TMBIM6, which act as indispensable co-

843   factors in the induction of NRF-2 signalling (Itoh et al., 1997; Katsuoka and Yamamoto, 2016;

844   Kim et al., 2020; Lee et al., 2007). Accompanying SARS-CoV-2-mediated downregulation of

845   NRF-2 signalling co-factors was the downregulation of NRF-2 target proteins. JQ-1

846   administration induced an upregulation of MAFK, TMBIM6, and NRF-2 target proteins, with a

847   more pronounced effect in the presence of infection. These data complement SARS-CoV-2-

848   and JQ-1-mediated differential regulation of NRF-2 TF activity and suggest that both SARS-

849   CoV-2 infection and JQ-1 administration regulate NRF-2 TF activity by modulating the

850   expression of its signalling co-factors and not NRF-2 expression *per se*. Suppression of NRF-2-

851   mediated cytoprotective response in biopsies from COVID-19 patients (Olagnier et al., 2020)

852   supports the biological plausibility of our data.

853   DMF- and 4-OI-mediated induction of NRF-2-driven cytoprotective protective response

854   with anti-SARS-CoV-2 activity (Olagnier et al., 2020) and known JQ-1-mediated induction of

855 NRF-2 signalling (Lv et al., 2022), prompted us to pursue the effect of JQ-1-mediated

856 induction of NRF-2 signalling in the context of JQ-1-mediated anti-SARS-CoV-2 activity.

857 Partial antagonism of JQ-1-mediated anti-SARS-CoV-2 activity by ML385, a specific inhibitor

858 of NRF-2 (Singh et al., 2016), suggest that induction of NRF-2 signalling by JQ-1

859 administration contributes to JQ-1-mediated anti-SARS-CoV-2 activity, which is consistent

860 with NRF-2-mediated anti-SARS-CoV-2 reported in the context DMF- and 4-OI-mediated

861 induction (Olagnier et al., 2020). The combination of JQ-1-mediated downregulation of ACE2

862 expression and induction of NRF-2 signalling shown in our study, suggest that JQ-1 exhibits a

863 pleiotropic anti-SARS-CoV-2 activity that affects multiple steps of the viral replication cycle.

864 How exactly JQ-1-mediated induction of NRF-2 signalling exerts an anti-SARS-CoV-2

865 activity remains unknown. Olagnier et al. proposed that the induction of hypoxia-inducible-

866 factor-1-alpha (HIF-1α) gene expression program induced by 4-OI administration, which was

867 downregulated in biopsies from COVID-19 patients along with NRF-2 signalling pathway,

868 potentially contribute to NRF-2-mediated antiviral cytoprotective response (Olagnier et al.,

869 2020). In contrast, Codo. et al. reported that SARS-CoV-2-mediated induction of ROS

870 stabilises HIF-1α to induce its gene expression program that promotes glycolysis to sustain

871 SARS-CoV-2 replication in monocytes (Codo et al., 2020). Consistent with the later report, we

872 found induction of HIF-1α TF activity following SARS-CoV-2 infection in Calu-3 cells.

873 Furthermore, irrespective of infection, JQ-1 administration also induced HIF-1α TF

874 activity. Downregulation of HIF-1α TF activity in control groups suggest that both SARS-CoV-

875 2 infection and JQ-1 administration induce HIF-1α signalling. This is consistent with the idea

876 of alternative JQ-1-driven HIF-1α TF activity-inducing mechanisms that are independent of

877 SARS-CoV-2-mediated ROS production and argues against the potential effect of HIF-1α-

878 mediated signalling in NRF-2-induced anti-SARS-CoV-2 activity proposed elsewhere

879 (Olagnier et al., 2020) . Alternatively, NRF-2 signalling induces the expression of a

880 cytoprotective enzyme called heme-oxygenase-1 (HO-1) (Olagnier et al., 2020; Wagener et al.,

881 2020), which catalyses the catabolism of heme into biliverdin, iron, and carbon monoxide (CO)

882 (Dunn et al., 2014). Interestingly, the products of HO-1-mediated heme catabolism exhibit a

883 broad-spectrum antiviral activity (Espinoza et al., 2017).

884 Of particular interest, prophylactic administration of free iron and biliverdin to Vero E6

885 cells prior to infection inhibited SARS-CoV-2 replication (Kim et al., 2021), In contrast,

886 despite binding to SARS-CoV-2-S protein with nanomolar affinity and dampening spike

887 interactions with neutralising antibodies, administration of 100μM biliverdin at the time of

888 infection did not inhibit infection of Vero E6 cells by SARS-CoV-2 (Rosa et al., 2021). These

889   studies (Kim et al., 2021; Rosa et al., 2021) suggest that like JQ-1, biliverdin-induced anti-

890   SARS-CoV-2 activity is directed at the host and not the infecting virions. This is consistent

891   with the maintenance of infection efficiency by the virions secreted under JQ-1 treatment.

892   Taken together, these studies highlight the mechanism underlying NRF-2-mediated anti-SARS-

893   CoV-2 activity, which itself remains to be fully unravelled.

894   Immune selection of SARS-CoV-2 has led to the emergence of VOCs bearing an

895   arsenal of mutations in the spike and other viral proteins, which confer immune evasion

896   capabilities and transmission superiority (Tuekprakhon et al., 2022; Willett et al., 2022).

897   SARS-CoV-2 adaptation to virus-directed antivirals such as remdesivir (RDV) has been

898   reported *in vitro* (Stevens et al., 2022; Szemiel et al., 2021) and *in vivo* (Heyer et al., 2022).

899   Here, as early as passage one (P1) under JQ-1 selection, SARS-CoV-2 RNA copies and

900   infectious titers increased in the supernatant and reached a plateau that was maintained across

901   14 passages despite the subsequent two-fold escalations of JQ-1 concentrations. Compared to

902   the parental strain, JQ-1-selected, and to a lesser extent also DMSO-selected, SARS-CoV-2

903   virions showed reduced sensitivity to JQ-1 treatment in Calu-3 cells. These data suggest that

904   passaging under DMSO, and even more under JQ-1, induced the emergence of SARS-CoV-2

905   variants with enhanced viral fitness and reduced sensitivity to JQ-1, unlike the acquisition of

906   resistance to RDV that led to viral replication defect *in vitro* (Stevens et al., 2022; Szemiel et

907   al., 2021).

908   NGS analysis of SARS-CoV-2 virions passaged under JQ-1 treatment revealed

909   acquisition of a premature stop codon corresponding to position six of ORF6, (ORF6^{D6STOP}

910   mutation), a mutation that was less pronounced in DMSO-selected virions. Like JQ-1, SARS-

911   CoV-2-ORF6 antagonises IFN signalling in infected cells (Miorin et al., 2020; Schroeder et al.,

912   2021; Xia et al., 2020). This IFN signalling-repressive effect of JQ-1 may have minimised the

913   need for ORF6-mediated repression of IFN signalling and promoted ORF6 trade-offs. This is

914   consistent with the early emergence of SARS-CoV-2 variants harbouring an in-frame deletion

915   in ORF6 following passaging in IFN-deficient Vero E6 cells (Riojas et al., 2020). In contrast,

916   replication of virions passaged under DMSO are expected to benefit from preserving the

917   ORF6-mediated antagonism of IFN signalling. Investigation of how the acquisition of

918   ORF6^{D6STOP} mutation mediates resistance to JQ-1-mediated antiviral activity and whether this

919   ORF6 trade-off constitutes an antagonistic pleiotropy by enhancing sensitivity to IFN treatment

920   is warranted. Together, these data suggest that acquisition of the ORF6^{D6STOP} mutation is not

921   uniquely induced by JQ-1 treatment, but gains more dominance after encountering an IFN-

922   deficient milieu induced by JQ-1 treatment.

923   The accumulating evidence from our study and previous studies (Gilham et al., 2021;

924 Mills et al., 2021; Samelson et al., 2022; Vann et al., 2022) show that iBETs exhibit an anti-

925 SARS-CoV-2 activity when administered prophylactically and not therapeutically (Chen et al.,

926 2022). Whether SARS-CoV-2 infection counteracts JQ-1-mediated infection barriers or

927 acquires alternative capabilities to infect and replicate in the host remains to be addressed in

928 future studies. Interestingly, in one study (Chen et al., 2022), administration of iBETs at the

929 time of infection, as opposed to pre-treatment, resulted in absence of an inhibitory effect and

930 even exacerbation of SARS-CoV-2 replication. In line with this report, JQ-1 displayed no

931 antiviral activity when administered in a therapeutic set-up in our study. The proviral effect of

932 therapeutically administered JQ-1 reported by (Chen et al., 2022), which is absent in our study,

933 may be related to different time points of sample harvest following infection (48 versus 24

934 hours, respectively). Since SARS-CoV-2 infection potently suppresses NRF-2-mediated

935 antiviral cytoprotection responses (Olagnier et al., 2020), subsequent and long-term JQ-1

936 administration may be unable to revert this effect, respectively, resulting in SARS-CoV-2-

937 mediated nullification of JQ-1-mediated anti-SARS-CoV-2 activity. Together, these data evoke

938 questions about the clinical suitability for both prophylactic and therapeutic administration of

939 JQ-1 (and likely other iBETs) in the context of COVID-19 and illuminate the potential hurdles

940 that iBETs will have to overcome in order to improve disease prognosis.

941

952 **AUTHOR CONTRIBUTIONS**

953 B. Mhle. and C.G. conceived the study and designed the experiments. B. Mhle., S.Sten., J.J.,

954 A.R., J.H. and N.H. performed the experiments. R.O., S. Schr., U.M. and D.N. provided the

955 material. B. Mhle., D.P., J.M.W., F.Z., B. Mue., T.C.J. and C.G. analysed the data. B. Mhle.

956   and C.G. drafted the manuscript. M.A.M., C.D., A.P., V.T., D.N., G.S., D.B., and C.G.

957   supervised the research. All authors reviewed and edited the manuscript.

958   **CONFLICT OF INTERESTS**

959   The authors declare no conflict of interests

960   **REFERENCES**

961   Acosta Lopez, M.J., Trevisson, E., Canton, M., Vazquez-Fonseca, L., Morbidoni, V.,

962   Baschiera, E., Frasson, C., Pelosi, L., Rascalou, B., Desbats, M.A., et al. (2019). Vanillic Acid

963   Restores Coenzyme Q Biosynthesis and ATP Production in Human Cells Lacking COQ6.

964   Oxid. Med. Cell. Longev. *2019*, 3904905. .

965   Agarwal, S., Nikolai, B., Yamaguchi, T., Lech, P., and Somia, N.V. (2006). Construction and

966   use of retroviral vectors encoding the toxic gene barnase. Mol. Ther. *14*, 555–563. .

967   Auboeuf, D., Dowhan, D.H., Kang, Y.K., Larkin, K., Lee, J.W., Berget, S.M., and O'Malley,

968   B.W. (2004). Differential recruitment of nuclear receptor coactivators may determine

969   alternative RNA splice site choice in target genes. Proc. Natl. Acad. Sci. U. S. A. *101*, 2270–

970   2274. .

971   Bailey, T.L. (2011). DREME: motif discovery in transcription factor ChIP-seq data.

972   Bioinformatics *27*, 1653–1659. .

973   Bailey, T.L., Johnson, J., Grant, C.E., and Noble, W.S. (2015). The MEME Suite. Nucleic

974   Acids Res. *43*, W39–W49. .

975   Balistreri, G., Horvath, P., Schweingruber, C., Zünd, D., McInerney, G., Merits, A.,

976   Mühlemann, O., Azzalin, C., and Helenius, A. (2014). The host nonsense-mediated mRNA

977   decay pathway restricts Mammalian RNA virus replication. Cell Host Microbe *16*, 403–411. .

978   Banerjee, A.K., Blanco, M.R., Bruce, E.A., Honson, D.D., Chen, L.M., Chow, A., Bhat, P.,

979   Ollikainen, N., Quinodoz, S.A., Loney, C., et al. (2020). SARS-CoV-2 Disrupts Splicing,

980   Translation, and Protein Trafficking to Suppress Host Defenses. Cell *183*, 1325–1339.e21. .

981   Benjamini, Y., and Hochberg, Y. (1995). Controlling the false discovery rate: A practical and

982   powerful approach to multiple testing. J. R. Stat. Soc. *57*, 289–300. .

983   Brann, D.H., Tsukahara, T., Weinreb, C., Lipovsek, M., Van den Berge, K., Gong, B., Chance,

984   R., Macaulay, I.C., Chou, H.-J., Fletcher, R.B., et al. (2020). Non-neuronal expression of

985   SARS-CoV-2 entry genes in the olfactory system suggests mechanisms underlying COVID-19-

986   associated anosmia. Sci Adv *6*. https://doi.org/10.1126/sciadv.abc5801.

987   Buenrostro, J.D., Giresi, P.G., Zaba, L.C., Chang, H.Y., and Greenleaf, W.J. (2013).

988   Transposition of native chromatin for fast and sensitive epigenomic profiling of open

989   chromatin, DNA-binding proteins and nucleosome position. Nat. Methods *10*, 1213–1218. .

990   Bülow Anderberg, S., Luther, T., Berglund, M., Larsson, R., Rubertsson, S., Lipcsey, M.,

991   Larsson, A., Frithiof, R., and Hultström, M. (2021). Increased levels of plasma cytokines and

992   correlations to organ failure and 30-day mortality in critically ill Covid-19 patients. Cytokine

993   *138*, 155389. .

994   Caamaño, J.H., Rizzo, C.A., Durham, S.K., Barton, D.S., Raventós-Suárez, C., Snapper, C.M.,

995   and Bravo, R. (1998). Nuclear Factor (NF)-κB2 (p100/p52) Is Required for Normal Splenic

996   Microarchitecture and B Cell–mediated Immune Responses. Journal of Experimental Medicine

997   *187*, 185–196. https://doi.org/10.1084/jem.187.2.185.

998   Chen, I.P., Longbotham, J.E., McMahon, S., Suryawanshi, R.K., Khalid, M.M., Taha, T.Y.,

999   Tabata, T., Hayashi, J.M., Soveg, F.W., Carlson-Stevermer, J., et al. (2022). Viral E protein

1000   neutralizes BET protein-mediated post-entry antagonism of SARS-CoV-2. Cell Rep. *40*,

1001   111088. .

1002   Cheung, K.L., Kim, C., and Zhou, M.-M. (2021). The Functions of BET Proteins in Gene

1003   Transcription of Biology and Diseases. Front Mol Biosci *8*, 728777. .

1004   Codo, A.C., Davanzo, G.G., Monteiro, L. de B., de Souza, G.F., Muraro, S.P., Virgilio-da-

1005   Silva, J.V., Prodonoff, J.S., Carregari, V.C., de Biagi Junior, C.A.O., Crunfli, F., et al. (2020).

1006   Elevated Glucose Levels Favor SARS-CoV-2 Infection and Monocyte Response through a

1007   HIF-1α/Glycolysis-Dependent Axis. Cell Metab. *32*, 437–446.e5. .

1008   Corces, M.R., Trevino, A.E., Hamilton, E.G., Greenside, P.G., Sinnott-Armstrong, N.A.,

1009   Vesuna, S., Satpathy, A.T., Rubin, A.J., Montine, K.S., Wu, B., et al. (2017). An improved

1010   ATAC-seq protocol reduces background and enables interrogation of frozen tissues. Nat.

1011   Methods *14*, 959–962. .

1012   Corman, V.M., Landt, O., Kaiser, M., Molenkamp, R., Meijer, A., Chu, D.K., Bleicker, T.,

1013   Brünink, S., Schneider, J., Schmidt, M.L., et al. (2020). Detection of 2019 novel coronavirus

1014   (2019-nCoV) by real-time RT-PCR. Euro Surveill. *25*. https://doi.org/10.2807/1560-

1015   7917.ES.2020.25.3.2000045.

1016   De Rijck, J., de Kogel, C., Demeulemeester, J., Vets, S., El Ashkar, S., Malani, N., Bushman,

1017   F.D., Landuyt, B., Husson, S.J., Busschots, K., et al. (2013). The BET family of proteins

1018   targets moloney murine leukemia virus integration near transcription start sites. Cell Rep. *5*,

1019   886–894. .

1020   Dobin, A., Davis, C.A., Schlesinger, F., Drenkow, J., Zaleski, C., Jha, S., Batut, P., Chaisson,

1021   M., and Gingeras, T.R. (2013). STAR: ultrafast universal RNA-seq aligner. Bioinformatics *29*,

1022   15–21. .

1023   Du, H., Zhao, Y., He, J., Zhang, Y., Xi, H., Liu, M., Ma, J., and Wu, L. (2016). YTHDF2

1024   destabilizes m(6)A-containing RNA through direct recruitment of the CCR4-NOT deadenylase

1025   complex. Nat. Commun. *7*, 12626. .

1026   Dunn, L.L., Midwinter, R.G., Ni, J., Hamid, H.A., Parish, C.R., and Stocker, R. (2014). New

1027   insights into intracellular locations and functions of heme oxygenase-1. Antioxid. Redox

1028   Signal. *20*, 1723–1742. .

1029   Elhasnaoui, J., Ferrero, G., Miano, V., Cutrupi, S., and De Bortoli, M. (2021). The Estrogen

1030   Receptor α Signaling Pathway Controls Alternative Splicing in the Absence of Ligands in

1031   Breast Cancer Cells. Cancers *13*. https://doi.org/10.3390/cancers13246261.

1032   Espinoza, J.A., González, P.A., and Kalergis, A.M. (2017). Modulation of Antiviral Immunity

1033   by Heme Oxygenase-1. Am. J. Pathol. *187*, 487–493. .

1034   Finkel, Y., Gluck, A., Nachshon, A., Winkler, R., Fisher, T., Rozman, B., Mizrahi, O.,

1035   Lubelsky, Y., Zuckerman, B., Slobodin, B., et al. (2021). SARS-CoV-2 uses a multipronged

1036   strategy to impede host protein synthesis. Nature *594*, 240–245. .

1037   Garcia-Alonso, L., Holland, C.H., Ibrahim, M.M., Turei, D., and Saez-Rodriguez, J. (2019).

1038   Benchmark and integration of resources for the estimation of human transcription factor

1039   activities. Genome Res. *29*, 1363–1375. .

1040   Gassen, N.C., Papies, J., Bajaj, T., Emanuel, J., Dethloff, F., Chua, R.L., Trimpert, J.,

1041   Heinemann, N., Niemeyer, C., Weege, F., et al. (2021). SARS-CoV-2-mediated dysregulation

1042   of metabolism and autophagy uncovers host-targeting antivirals. Nat. Commun. *12*, 3818. .

1043   Gilham, D., Smith, A.L., Fu, L., Moore, D.Y., Muralidharan, A., Reid, S.P.M., Stotz, S.C.,

1044   Johansson, J.O., Sweeney, M., Wong, N.C.W., et al. (2021). Bromodomain and Extraterminal

1045   Protein Inhibitor, Apabetalone (RVX-208), Reduces ACE2 Expression and Attenuates SARS-

1046   Cov-2 Infection In Vitro. Biomedicines *9*. https://doi.org/10.3390/biomedicines9040437.

1047   Gokhale, N.S., McIntyre, A.B.R., McFadden, M.J., Roder, A.E., Kennedy, E.M., Gandara, J.A.,

1048   Hopcraft, S.E., Quicke, K.M., Vazquez, C., Willer, J., et al. (2016). N6-Methyladenosine in

1049   Flaviviridae Viral RNA Genomes Regulates Infection. Cell Host Microbe *20*, 654–665. .

1050   Gonzales-van Horn, S.R., and Sarnow, P. (2017). Making the Mark: The Role of Adenosine

1051   Modifications in the Life Cycle of RNA Viruses. Cell Host Microbe *21*, 661–669. .

1052   Gordon, D.E., Jang, G.M., Bouhaddou, M., Xu, J., Obernier, K., White, K.M., O'Meara, M.J.,

1053   Rezelj, V.V., Guo, J.Z., Swaney, D.L., et al. (2020). A SARS-CoV-2 protein interaction map

1054   reveals targets for drug repurposing. Nature *583*, 459–468. .

1055   Guarnieri, J.W., Dybas, J.M., Fazelinia, H., Kim, M.S., Frere, J., Zhang, Y., Albrecht, Y.S.,

1056   Murdock, D.G., Angelin, A., Singh, L.N., et al. (2022). Targeted Down Regulation Of Core

1057   Mitochondrial Genes During SARS-CoV-2 Infection. bioRxiv

1058   https://doi.org/10.1101/2022.02.19.481089.

1059   Hajmirza, A., Emadali, A., Gauthier, A., Casasnovas, O., Gressin, R., and Callanan, M.B.

1060   (2018). BET Family Protein BRD4: An Emerging Actor in NFκB Signaling in Inflammation

1061   and Cancer. Biomedicines *6*. https://doi.org/10.3390/biomedicines6010016.

1062   He, F., Ru, X., and Wen, T. (2020). NRF2, a Transcription Factor for Stress Response and

1063   Beyond. Int. J. Mol. Sci. *21*. https://doi.org/10.3390/ijms21134777.

1064   Heyer, A., Günther, T., Robitaille, A., Lütgehetmann, M., Addo, M.M., Jarczak, D., Kluge, S.,

1065   Aepfelbacher, M., Schulze zurWiesch, J., Fischer, N., et al. (2022). Remdesivir-induced

1066   emergence of SARS-CoV2 variants in patients with prolonged infection. Cell Reports Medicine

1067   100735. .

1068   Hoffmann, M., Kleine-Weber, H., Schroeder, S., Krüger, N., Herrler, T., Erichsen, S.,

1069   Schiergens, T.S., Herrler, G., Wu, N.-H., Nitsche, A., et al. (2020). SARS-CoV-2 Cell Entry

1070   Depends on ACE2 and TMPRSS2 and Is Blocked by a Clinically Proven Protease Inhibitor.

1071   Cell *181*, 271–280.e8. .

1072   Hu, J., Gao, Q., He, C., Huang, A., Tang, N., and Wang, K. (2020). Development of cell-based

1073   pseudovirus entry assay to identify potential viral entry inhibitors and neutralizing antibodies

1074   against SARS-CoV-2. Genes Dis *7*, 551–557. .

1075   Huang, B., Yang, X.-D., Zhou, M.-M., Ozato, K., and Chen, L.-F. (2009). Brd4 coactivates

1076   transcriptional activation of NF-kappaB via specific binding to acetylated RelA. Mol. Cell.

1077   Biol. *29*, 1375–1387. .

1078   Itoh, K., Chiba, T., Takahashi, S., Ishii, T., Igarashi, K., Katoh, Y., Oyake, T., Hayashi, N.,

1079   Satoh, K., Hatayama, I., et al. (1997). An Nrf2/Small Maf Heterodimer Mediates the Induction

1080   of Phase II Detoxifying Enzyme Genes through Antioxidant Response Elements. Biochemical

1081   and Biophysical Research Communications *236*, 313–322.

1082   https://doi.org/10.1006/bbrc.1997.6943.

1083   Jochim, N., Gerhard, R., Just, I., and Pich, A. (2011). Impact of clostridial glucosylating toxins

1084   on the proteome of colonic cells determined by isotope-coded protein labeling and LC-MALDI.

1085   Proteome Sci. *9*, 48. .

1086   Katsuoka, F., and Yamamoto, M. (2016). Small Maf proteins (MafF, MafG, MafK): History,

1087   structure and function. Gene *586*, 197–205. https://doi.org/10.1016/j.gene.2016.03.058.

1088   Kee, J., Thudium, S., Renner, D., Glastad, K., Palozola, K., Zhang, Z., Li, Y., Cesare, J., Lan,

1089   Y., Truitt, R., et al. (2021). SARS-CoV-2 ORF8 encoded protein contains a histone mimic,

1090   disrupts chromatin regulation, and enhances replication.

1091   Kim, D.-H., Ahn, H.-S., Go, H.-J., Kim, D.-Y., Kim, J.-H., Lee, J.-B., Park, S.-Y., Song, C.-S.,

1092   Lee, S.-W., Ha, S.-D., et al. (2021). Hemin as a novel candidate for treating COVID-19 via

1093   heme oxygenase-1 induction. Sci. Rep. *11*, 21462. .

1094   Kim, H.-K., Bhattarai, K.R., Junjappa, R.P., Ahn, J.H., Pagire, S.H., Yoo, H.J., Han, J., Lee,

1095   D., Kim, K.-W., Kim, H.-R., et al. (2020). TMBIM6/BI-1 contributes to cancer progression

1096   through assembly with mTORC2 and AKT activation. Nat. Commun. *11*, 4012. .

1097   Lam, M.T.Y., Duttke, S.H., Odish, M.F., Le, H.D., Hansen, E.A., Nguyen, C.T., Trescott, S.,

1098   Kim, R., Deota, S., Chang, M.W., et al. (2021). Profiling Transcription Initiation in Peripheral

1099   Leukocytes Reveals Severity-Associated Cis-Regulatory Elements in Critical COVID-19.

1100   bioRxiv https://doi.org/10.1101/2021.08.24.457187.

1101   Lara-Ureña, N., and García-Domínguez, M. (2021). Relevance of BET Family Proteins in

1102   SARS-CoV-2 Infection. Biomolecules *11*. https://doi.org/10.3390/biom11081126.

1103   Lau, S.K.P., Woo, P.C.Y., Li, K.S.M., Huang, Y., Tsoi, H.-W., Wong, B.H.L., Wong, S.S.Y.,

1104   Leung, S.-Y., Chan, K.-H., and Yuen, K.-Y. (2005). Severe acute respiratory syndrome

1105   coronavirus-like virus in Chinese horseshoe bats. Proc. Natl. Acad. Sci. U. S. A. *102*, 14040–

1106   14045. .

1107   Lee, G.-H., Kim, H.-K., Chae, S.-W., Kim, D.-S., Ha, K.-C., Cuddy, M., Kress, C., Reed, J.C.,

1108   Kim, H.-R., and Chae, H.-J. (2007). Bax inhibitor-1 regulates endoplasmic reticulum stress-

1109   associated reactive oxygen species and heme oxygenase-1 expression. J. Biol. Chem. *282*,

1110   21618–21628. .

1111   Lee, J.S., Park, S., Jeong, H.W., Ahn, J.Y., Choi, S.J., Lee, H., Choi, B., Nam, S.K., Sa, M.,

1112   Kwon, J.-S., et al. (2020). Immunophenotyping of COVID-19 and influenza highlights the role

1113   of type I interferons in development of severe COVID-19. Sci Immunol *5*.

1114   https://doi.org/10.1126/sciimmunol.abd1554.

1115   Lichinchi, G., Zhao, B.S., Wu, Y., Lu, Z., Qin, Y., He, C., and Rana, T.M. (2016). Dynamics of

1116   Human and Viral RNA Methylation during Zika Virus Infection. Cell Host Microbe *20*, 666–

1117   673. .

1118   Love, M.I., Huber, W., and Anders, S. (2014). Moderated estimation of fold change and

1119   dispersion for RNA-seq data with DESeq2. Genome Biol. *15*, 550. .

1120   Lv, Y., Lv, X., Zhang, J., Cao, G., Xu, C., Zhang, B., and Lin, W. (2022). BRD4 Targets the

1121   KEAP1-Nrf2-G6PD Axis and Suppresses Redox Metabolism in Small Cell Lung Cancer.

1122   Antioxidants (Basel) *11*. https://doi.org/10.3390/antiox11040661.

1123   de Melo, G.D., Lazarini, F., Levallois, S., Hautefort, C., Michel, V., Larrous, F., Verillaud, B.,

1124   Aparicio, C., Wagner, S., Gheusi, G., et al. (2021). COVID-19-related anosmia is associated

1125   with viral persistence and inflammation in human olfactory epithelium and brain infection in

1126   hamsters. Sci. Transl. Med. *13*. https://doi.org/10.1126/scitranslmed.abf8396.

1127   Mhlekude, B., Lenman, A., Sidoyi, P., Joseph, J., Kruppa, J., Businge, C.B., Mdaka, M.L.,
1128   Konietschke, F., Pich, A., Gerold, G., et al. (2021). The barrier functions of crude cervical
1129   mucus plugs against HIV-1 infection in the context of cell-free and cell-to-cell transmission.
1130   AIDS *35*, 2105–2117. .

1131   Mills, R.J., Humphrey, S.J., Fortuna, P.R.J., Lor, M., Foster, S.R., Quaife-Ryan, G.A.,
1132   Johnston, R.L., Dumenil, T., Bishop, C., Rudraraju, R., et al. (2021). BET inhibition blocks
1133   inflammation-induced cardiac dysfunction and SARS-CoV-2 infection. Cell *184*, 2167–
1134   2182.e22. .

1135   Miorin, L., Kehrer, T., Sanchez-Aparicio, M.T., Zhang, K., Cohen, P., Patel, R.S., Cupic, A.,
1136   Makio, T., Mei, M., Moreno, E., et al. (2020). SARS-CoV-2 Orf6 hijacks Nup98 to block
1137   STAT nuclear import and antagonize interferon signaling. Proc. Natl. Acad. Sci. U. S. A. *117*,
1138   28344–28354. .

1139   Niemeyer, D., Schroeder, S., Friedmann, K., Weege, F., Trimpert, J., Richter, A., Stenzel, S.,
1140   Jansen, J., Emanuel, J., Kazmierski, J., et al. (2021). Post-entry, spike-dependent replication
1141   advantage of B.1.1.7 and B.1.617.2 over B.1 SARS-CoV-2 in an ACE2-deficient human lung
1142   cell line.

1143   Nilsson-Payant, B.E., Uhl, S., Grimont, A., Doane, A.S., Cohen, P., Patel, R.S., Higgins, C.A.,
1144   Acklin, J.A., Bram, Y., Chandar, V., et al. (2021). The NF-κB Transcriptional Footprint Is
1145   Essential for SARS-CoV-2 Replication. J. Virol. *95*, e0125721. .

1146   Olagnier, D., Farahani, E., Thyrsted, J., Blay-Cadanet, J., Herengt, A., Idorn, M., Hait, A.,
1147   Hernaez, B., Knudsen, A., Iversen, M.B., et al. (2020). SARS-CoV2-mediated suppression of
1148   NRF2-signaling reveals potent antiviral and anti-inflammatory activity of 4-octyl-itaconate and
1149   dimethyl fumarate. Nat. Commun. *11*, 4938. .

1150   Oldfield, A.J., Yang, P., Conway, A.E., Cinghu, S., Freudenberg, J.M., Yellaboina, S., and
1151   Jothi, R. (2014). Histone-fold domain protein NF-Y promotes chromatin accessibility for cell
1152   type-specific master transcription factors. Mol. Cell *55*, 708–722. .

1153   Oldfield, A.J., Henriques, T., Kumar, D., Burkholder, A.B., Cinghu, S., Paulet, D., Bennett,
1154   B.D., Yang, P., Scruggs, B.S., Lavender, C.A., et al. (2019). NF-Y controls fidelity of

1155   transcription initiation at gene promoters through maintenance of the nucleosome-depleted

1156   region. Nat. Commun. *10*, 3072. .

1157   Park, A., and Iwasaki, A. (2020). Type I and Type III Interferons – Induction, Signaling,

1158   Evasion, and Application to Combat COVID-19. Cell Host & Microbe *27*, 870–878.

1159   https://doi.org/10.1016/j.chom.2020.05.008.

1160   Patel, M.C., Debrosse, M., Smith, M., Dey, A., Huynh, W., Sarai, N., Heightman, T.D.,

1161   Tamura, T., and Ozato, K. (2013). BRD4 coordinates recruitment of pause release factor P-

1162   TEFb and the pausing complex NELF/DSIF to regulate transcription elongation of interferon-

1163   stimulated genes. Mol. Cell. Biol. *33*, 2497–2507. .

1164   Qiu, C., Cui, C., Hautefort, C., Haehner, A., Zhao, J., Yao, Q., Zeng, H., Nisenbaum, E.J., Liu,

1165   L., Zhao, Y., et al. (2020). Olfactory and Gustatory Dysfunction as an Early Identifier of

1166   COVID-19 in Adults and Children: An International Multicenter Study. Otolaryngol. Head

1167   Neck Surg. *163*, 714–721. .

1168   Ramasamy, S., and Subbian, S. (2021). Critical Determinants of Cytokine Storm and Type I

1169   Interferon Response in COVID-19 Pathogenesis. Clin. Microbiol. Rev. *34*.

1170   https://doi.org/10.1128/CMR.00299-20.

1171   Rana, M., Dong, J., Robertson, M.J., Basil, P., Coarfa, C., and Weigel, N.L. (2021). Androgen

1172   receptor and its splice variant, AR-V7, differentially induce mRNA splicing in prostate cancer

1173   cells. Scientific Reports *11*. https://doi.org/10.1038/s41598-021-81164-0.

1174   Riojas, M.A., Frank, A.M., Puthuveetil, N.P., Flores, B., Parker, M., King, S.P., Peiris, M.,

1175   Chu, D.K.W., Benton, B., Bradford, R., et al. (2020). A Rare Deletion in SARS-CoV-2 ORF6

1176   Dramatically Alters the Predicted Three-Dimensional Structure of the Resultant Protein.

1177   bioRxiv https://doi.org/10.1101/2020.06.09.134460.

1178   Rosa, A., Pye, V.E., Graham, C., Muir, L., Seow, J., Ng, K.W., Cook, N.J., Rees-Spear, C.,

1179   Parker, E., Dos Santos, M.S., et al. (2021). SARS-CoV-2 can recruit a heme metabolite to

1180   evade antibody immunity. Sci Adv *7*. https://doi.org/10.1126/sciadv.abg7607.

1181   Samelson, A.J., Tran, Q.D., Robinot, R., Carrau, L., Rezelj, V.V., Kain, A.M., Chen, M.,

1182   Ramadoss, G.N., Guo, X., Lim, S.A., et al. (2022). BRD2 inhibition blocks SARS-CoV-2

1183   infection by reducing transcription of the host cell receptor ACE2. Nat. Cell Biol. *24*, 24–34. .

1184 Schoeman, D., and Fielding, B.C. (2020). Is There a Link Between the Pathogenic Human
1185 Coronavirus Envelope Protein and Immunopathology? A Review of the Literature. Front.
1186 Microbiol. *11*, 2086. .

1187 Schroeder, S., Pott, F., Niemeyer, D., Veith, T., Richter, A., Muth, D., Goffinet, C., Müller,
1188 M.A., and Drosten, C. (2021). Interferon antagonism by SARS-CoV-2: a functional study using
1189 reverse genetics. Lancet Microbe *2*, e210–e218. .

1190 Shah, K., Gagliano, T., Garland, L., O'Hanlon, T., Bortolotti, D., Gentili, V., Rizzo, R.,
1191 Giamas, G., and Dean, M. (2020). Androgen receptor signaling regulates the transcriptome of
1192 prostate cancer cells by modulating global alternative splicing. Oncogene *39*, 6172–6189. .

1193 Shorstova, T., Foulkes, W.D., and Witcher, M. (2021). Achieving clinical success with BET
1194 inhibitors as anti-cancer agents. Br. J. Cancer *124*, 1478–1490. .

1195 Silva, N.S.D., De Silva, N.S., Anderson, M.M., Carette, A., Silva, K., Heise, N., Bhagat, G.,
1196 and Klein, U. (2016). Transcription factors of the alternative NF-κB pathway are required for
1197 germinal center B-cell development. Proceedings of the National Academy of Sciences *113*,
1198 9063–9068. https://doi.org/10.1073/pnas.1602728113.

1199 Singh, A., Venkannagari, S., Oh, K.H., Zhang, Y.-Q., Rohde, J.M., Liu, L., Nimmagadda, S.,
1200 Sudini, K., Brimacombe, K.R., Gajghate, S., et al. (2016). Small Molecule Inhibitor of NRF2
1201 Selectively Intervenes Therapeutic Resistance in KEAP1-Deficient NSCLC Tumors. ACS
1202 Chem. Biol. *11*, 3214–3225. .

1203 Stark, and Brown DiffBind: differential binding analysis of ChIP-Seq peak data. R Package
1204 Version.

1205 Stathis, A., and Bertoni, F. (2018). BET Proteins as Targets for Anticancer Treatment. Cancer
1206 Discov. *8*, 24–36. .

1207 Stevens, L.J., Pruijssers, A.J., Lee, H.W., Gordon, C.J., Tchesnokov, E.P., Gribble, J., George,
1208 A.S., Hughes, T.M., Lu, X., Li, J., et al. (2022). Mutations in the SARS-CoV-2 RNA
1209 dependent RNA polymerase confer resistance to remdesivir by distinct mechanisms. Sci.
1210 Transl. Med. eabo0718. .

1211 Stewart, S.A., Dykxhoorn, D.M., Palliser, D., Mizuno, H., Yu, E.Y., An, D.S., Sabatini, D.M.,

1212   Chen, I.S.Y., Hahn, W.C., Sharp, P.A., et al. (2003). Lentivirus-delivered stable gene silencing

1213   by RNAi in primary cells. RNA *9*, 493–501. .

1214   Suarez-Alvarez, B., Rodriguez, R.M., Ruiz-Ortega, M., and Lopez-Larrea, C. (2017). BET

1215   Proteins: An Approach to Future Therapies in Transplantation. Am. J. Transplant *17*, 2254–

1216   2262. .

1217   Szemiel, A.M., Merits, A., Orton, R.J., MacLean, O.A., Pinto, R.M., Wickenhagen, A., Lieber,

1218   G., Turnbull, M.L., Wang, S., Furnon, W., et al. (2021). In vitro selection of Remdesivir

1219   resistance suggests evolutionary predictability of SARS-CoV-2. PLoS Pathog. *17*, e1009929. .

1220   Thi Nhu Thao, T., Labroussaa, F., Ebert, N., V'kovski, P., Stalder, H., Portmann, J., Kelly, J.,

1221   Steiner, S., Holwerda, M., Kratzel, A., et al. (2020). Rapid reconstruction of SARS-CoV-2

1222   using a synthetic genomics platform. Nature *582*, 561–565. .

1223   Tuekprakhon, A., Nutalai, R., Dijokaite-Guraliuc, A., Zhou, D., Ginn, H.M., Selvaraj, M., Liu,

1224   C., Mentzer, A.J., Supasa, P., Duyvesteyn, H.M.E., et al. (2022). Antibody escape of SARS-

1225   CoV-2 Omicron BA.4 and BA.5 from vaccine and BA.1 serum. Cell *185*, 2422–2433.e13. .

1226   Vann, K.R., Acharya, A., Jang, S.M., Lachance, C., Zandian, M., Holt, T.A., Smith, A.L.,

1227   Pandey, K., Durden, D.L., El-Gamal, D., et al. (2022). Binding of the SARS-CoV-2 envelope E

1228   protein to human BRD4 is essential for infection. Structure

1229   https://doi.org/10.1016/j.str.2022.05.020.

1230   Wada, M., Lokugamage, K.G., Nakagawa, K., Narayanan, K., and Makino, S. (2018). Interplay

1231   between coronavirus, a cytoplasmic RNA virus, and nonsense-mediated mRNA decay

1232   pathway. Proc. Natl. Acad. Sci. U. S. A. *115*, E10157–E10166. .

1233   Wagener, F.A.D.T.G., Pickkers, P., Peterson, S.J., Immenschuh, S., and Abraham, N.G. (2020).

1234   Targeting the Heme-Heme Oxygenase System to Prevent Severe Complications Following

1235   COVID-19 Infections. Antioxidants (Basel) *9*. https://doi.org/10.3390/antiox9060540.

1236   Wang, Y., and Hekimi, S. (2016). Understanding Ubiquinone. Trends Cell Biol. *26*, 367–378. .

1237   Wilk, A.J., Lee, M.J., Wei, B., Parks, B., Pi, R., Martínez-Colón, G.J., Ranganath, T., Zhao,

1238   N.Q., Taylor, S., Becker, W., et al. (2021). Multi-omic profiling reveals widespread

1239   dysregulation of innate immunity and hematopoiesis in COVID-19. J. Exp. Med. *218*.

1240   https://doi.org/10.1084/jem.20210582.

1241   Willett, B.J., Grove, J., MacLean, O.A., Wilkie, C., De Lorenzo, G., Furnon, W., Cantoni, D.,

1242   Scott, S., Logan, N., Ashraf, S., et al. (2022). SARS-CoV-2 Omicron is an immune escape

1243   variant with an altered cell entry pathway. Nat Microbiol https://doi.org/10.1038/s41564-022-

1244   01143-7.

1245   Wintjes, L.T.M., Kava, M., van den Brandt, F.A., van den Brand, M.A.M., Lapina, O.,

1246   Bliksrud, Y.T., Kulseth, M.A., Amundsen, S.S., Selberg, T.R., Ybema-Antoine, M., et al.

1247   (2021). A novel variant in COX16 causes cytochrome c oxidase deficiency, severe fatal

1248   neonatal lactic acidosis, encephalopathy, cardiomyopathy, and liver dysfunction. Hum. Mutat.

1249   *42*, 135–141. .

1250   Wölfel, R., Corman, V.M., Guggemos, W., Seilmaier, M., Zange, S., Müller, M.A., Niemeyer,

1251   D., Jones, T.C., Vollmar, P., Rothe, C., et al. (2020). Virological assessment of hospitalized

1252   patients with COVID-2019. Nature *581*, 465–469. .

1253   Wu, S.-Y., Nin, D.S., Lee, A.-Y., Simanski, S., Kodadek, T., and Chiang, C.-M. (2016). BRD4

1254   Phosphorylation Regulates HPV E2-Mediated Viral Transcription, Origin Replication, and

1255   Cellular MMP-9 Expression. Cell Rep. *16*, 1733–1748. .

1256   Xia, H., Cao, Z., Xie, X., Zhang, X., Chen, J.Y.-C., Wang, H., Menachery, V.D., Rajsbaum, R.,

1257   and Shi, P.-Y. (2020). Evasion of Type I Interferon by SARS-CoV-2. Cell Rep. *33*, 108234. .

1258   You, M., Chen, L., Zhang, D., Zhao, P., Chen, Z., Qin, E.-Q., Gao, Y., Davis, M.M., and Yang,

1259   P. (2021). Single-cell epigenomic landscape of peripheral immune cells reveals establishment

1260   of trained immunity in individuals convalescing from COVID-19. Nat. Cell Biol. *23*, 620–630.

1261   .

1262   Yu, G., Wang, L.-G., Han, Y., and He, Q.-Y. (2012). clusterProfiler: an R package for

1263   comparing biological themes among gene clusters. OMICS *16*, 284–287. .

1264   Zaki, A.M., van Boheemen, S., Bestebroer, T.M., Osterhaus, A.D.M.E., and Fouchier, R.A.M.

1265   (2012). Isolation of a novel coronavirus from a man with pneumonia in Saudi Arabia. N. Engl.

1266   J. Med. *367*, 1814–1820. .

1267   Zeng, F.Y., Chan, C.W.M., Chan, M.N., Chen, J.D., Chow, K.Y.C., Hon, C.C., Hui, K.H., Li,

1268   J., Li, V.Y.Y., Wang, C.Y., et al. (2003). The complete genome sequence of severe acute

1269   respiratory syndrome coronavirus strain HKU-39849 (HK-39). Exp. Biol. Med. *228*, 866–873. .

1270   Zhang, Y., Liu, T., Meyer, C.A., Eeckhoute, J., Johnson, D.S., Bernstein, B.E., Nusbaum, C.,

1271   Myers, R.M., Brown, M., Li, W., et al. (2008). Model-based analysis of ChIP-Seq (MACS).

1272   Genome Biol. *9*, R137. .

1273   Zufferey, R., Nagy, D., Mandel, R.J., Naldini, L., and Trono, D. (1997). Multiply attenuated

1274   lentiviral vector achieves efficient gene delivery in vivo. Nat. Biotechnol. *15*, 871–875. .

1275